APPLIED SCIENCES AND ENGINEERING

In vivo and in situ monitoring of doxorubicin pharmacokinetics with an implantable bioresorbable optical sensor

Martina Corsi[1], Elena Maurina[1], Salvatore Surdo[1], Eleonora Vandini[2], Eleonora Daini[2], Antonietta Vilella[2], Giuseppina Leo[2], Moein Farshchian[3], Giulia Grisendi[3], Giulia Golinelli[3], Massimo Dominici[3], Guido Bocci[4], Daniela Giuliani[2], Giuseppe Barillaro[1]*

Cancer treatment, particularly chemotherapy, requires balancing efficacy and toxicity. Although traditional monitoring methods can lead to suboptimal outcomes, emerging implantable chemical sensors can complement them by providing precise, real-time drug monitoring at tumor sites, although the technology remains in its early stages. Here, we introduce an ultrathin, bioresorbable implantable biosensor for real-time doxorubicin monitoring in vivo with high spatiotemporal resolution. The sensor amplifies the drug's fluorescence, enabling successful tracking of doxorubicin through the skin in live mice following intravenous injection. When paired with a reusable electronic patch, the biosensor facilitates seamless data collection and wireless transmission. A 3-month biocompatibility study, including systemic toxicity assessments, histological and blood analyses, confirms complete biodegradation with no observed toxicity. By directly measuring chemotherapeutic drug levels in tissues over time, our sensor enhances traditional monitoring methods, enabling clinicians to optimize dosing during cancer treatment and reduce the risk of locoregional recurrence following tumor removal.

INTRODUCTION

Chemotherapy stands as a cornerstone in the fight against cancer, its efficacy relying heavily on maintaining optimal drug concentrations within the body (*1*–*3*). Yet, the current methods for monitoring these concentrations often fall short, lacking the temporal and spatial precision needed for personalized treatment. Traditionally, the chemotherapy response of a tumor mass has been assessed through indirect measurements, such as periodic blood tests (e.g., measuring drug concentrations or specific biomarkers) (*4*–*6*) or imaging studies [e.g., positron emission tomography (PET) scans] (*7*). PET scans are used to assess tumor response to treatment, whereas blood tests are used to monitor patient's condition, detect toxicity, and prevent complications like neutropenia.

Therapeutic drug monitoring of chemotherapeutic drugs is widely used in clinical settings to optimize treatment by ensuring the drug concentrations remain within a therapeutic range while minimizing toxicity (*8*). Established analytical techniques based on liquid chromatography and mass spectrometry (*9*–*12*) are typically used for the quantification of chemotherapeutic drugs. These methods combine high sensitivity and specificity, allowing accurate measurements in serum, plasma, and other biological matrices, such as saliva (*11*) and tissue samples (*13*).

However, blood tests only provide systemic drug concentration levels, which may not reflect drug concentration at the tumor site. In addition, they typically offer data from single time points as repeated blood sampling can be invasive and inconvenient for patients in the clinical routine, which may not capture the complete pharmacokinetic profile. Although systemic monitoring remains widely used, complementary localized techniques, such as volumetric absorptive microsampling based on the collection of small blood samples (*14*, *15*), hold promise for providing tumor-specific pharmacokinetic insights in the future yet with limited temporal resolution.

Implantable bioresorbable chemical sensors offer the potential to monitor drug concentrations with high spatial and temporal precision over time directly at the tumor site; however, their development is still in its early stages. By providing continuous, site-specific data on chemotherapeutic drug concentration, implantable sensors would complement traditional systemic monitoring methods to empower clinicians to optimize treatment strategies. From adjusting dosages to modifying drug delivery mechanisms, these devices could offer a level of treatment's personalization that was once unimaginable. Moreover, their unique ability to biodegrade over time would ensure no lasting impact on the body, offering a safe and sustainable solution.

Over the past decade numerous implantable bioresorbable physical sensors have been developed to monitor various physiological parameters (*16*–*19*). From temperature and pressure to strain and motion, these sensors offer real-time data acquisition, enabling clinicians to gain insights into bodily functions with unprecedented accuracy and precision. Crafted from bioresorbable materials that gradually degrade within the body, these sensors eliminate the need for surgical removal, reducing patient discomfort and minimizing the risk of complications associated with long-term implants. An encapsulation layer protects the sensor during its operational lifetime and then gradually dissolves over time, eventually triggering the degradation of the sensor itself (*20*).

In contrast, implantable chemical sensors based on bioresorbable materials are limited in number. These sensors require contact with the biofluid and cannot be fully protected by an encapsulation layer, posing challenges for their stability and life span. Balancing the sensor's degradation rate with the desired sensing time frame

---

[1]Department of Information Engineering, University of Pisa, via G. Caruso 16, 56122 Pisa, Italy. [2]Department of Biomedical Metabolic and Neural Sciences, University of Modena and Reggio Emilia, via G. Campi 287, 41125 Modena, Italy. [3]Department of Medical and Surgical Science for Children and Adults, University Hospital of Modena and Reggio Emilia, Via del Pozzo, 71, 41124 Modena, Italy. [4]Department of Translational Research and New Technologies in Medicine and Surgery School of Medicine, University of Pisa, Via Risorgimento 36, 56126 Pisa, Italy.
*Corresponding author. Email: giuseppe.barillaro@unipi.it

while maintaining accuracy is a substantial challenge. Although a few examples of bioresorbable chemical sensors operating in vivo have been reported for ions and diatomic molecules (*20*–*25*), e.g., H^+, Ca^{2+}, and O_2, and small molecules, e.g., glucose (*26*) and dopamine (*21*, *27*), detecting drug molecules, e.g., chemotherapeutic, with bioresorbable sensors remains unexplored.

A limited number of studies (*13*, *28*–*30*) have been conducted on the use of nonresorbable implantable sensors for monitoring chemotherapeutic drugs in vivo, such as doxorubicin used in the treatment of leukemia, thyroid, breast, and bladder cancers (*31*). Doxorubicin operates by intercalating with DNA, not only stabilizing the topoisomerase II complex and inhibiting tumor cell division but also adversely dividing normal cells (*32*, *33*). Consequently, its use can result in severe adverse drug reactions including myelosuppression, fatigue, hair loss, nausea, and cardiac toxicity, thus limiting its long-term application (*31*, *34*). The maximum cumulative dose typically prescribed is 450/500 mg/m^2 (*35*), although precise dosing is imperative as overdosing heightens adverse drug reactions (*36*), whereas underdosing yields therapeutic failure (*37*). Arroyo-Currás *et al.* (*29*) reported on an electrochemical sensor using aptamers to monitor doxorubicin levels in vivo and over time, assessing its clearance from the circulatory system. The sensor is neither fully implantable nor bioresorbable. Harvey *et al.* (*28*) reported on an optical biosensor composed of single-walled carbon nanotubes functionalized with DNA to enable specific binding of doxorubicin by the nanotubes. The sensor responds to the presence of the drug with a red shift of the nanotube's fluorescence emission. The sensor is not bioresorbable, and its biocompatibility was not assessed in vivo.

In this study, we introduce a bioresorbable doxorubicin sensor designed for implantation at the surgical site, either after primary tumor removal or in cases where surgery is not feasible or recommended. The biosensor provides localized, real-time data on doxorubicin concentrations in the tissue at the implantation site following intravenous chemotherapy administration. The biosensor, as thin as 5 μm and composed entirely of bioresorbable materials, is tested in vivo in mice to demonstrate its ability to monitor free doxorubicin concentrations at the subcutaneous level with high spatial and temporal resolution, achieving a limit of detection (LoD) of 3 ng/ml. The sensor leverages the intrinsic fluorescence of doxorubicin as its output signal, which is amplified by two orders of magnitude within the sensor, enabling readout through the skin. Pairing of the sensor with a reusable electronic patch placed on the skin's surface facilitates real-time data collection and wireless transmission to a mobile device. The sensor's biocompatibility is assessed over 3 months in mice through in vivo systemic toxicity assessments and ex vivo histological and blood analyses. Complete biodegradation of the sensor was confirmed at euthanasia, 3 months after implantation, and no signs of systemic toxicity, histological, or biochemical alterations were observed in mice implanted with the sensor compared to controls.

RESULTS

Figure 1 illustrates the concept of monitoring doxorubicin in vivo with high spatial and temporal resolution using a bioresorbable sensor implanted in the subcutaneous tissue at the surgical site, following primary tumor removal. The sensor is paired with a reusable electronic patch placed on the skin's surface, facilitating real-time data collection and wireless transmission to a mobile device. Our approach leverages the fluorescence amplification of doxorubicin molecules selectively trapped by the biosensor. This amplification enables us to infer the drug concentration in the tissue by measuring the fluorescence intensity through the skin over time at the implantation site. After several days of operation, the sensor completely dissolves into safe by-products, eliminating need for retrieval through a secondary surgery.

The electronic patch, positioned over the sensor, activates doxorubicin fluorescence and measures its intensity through the skin. As a result, real-time data on drug concentration are generated and wirelessly transmitted to a mobile device for presentation and storage. The patch's circuitry is programmable to selectively query the sensor on demand and is designed to be reused multiple times with different sensors. The biosensor is designed to provide physicians with localized drug pharmacokinetic data at the tissue implantation

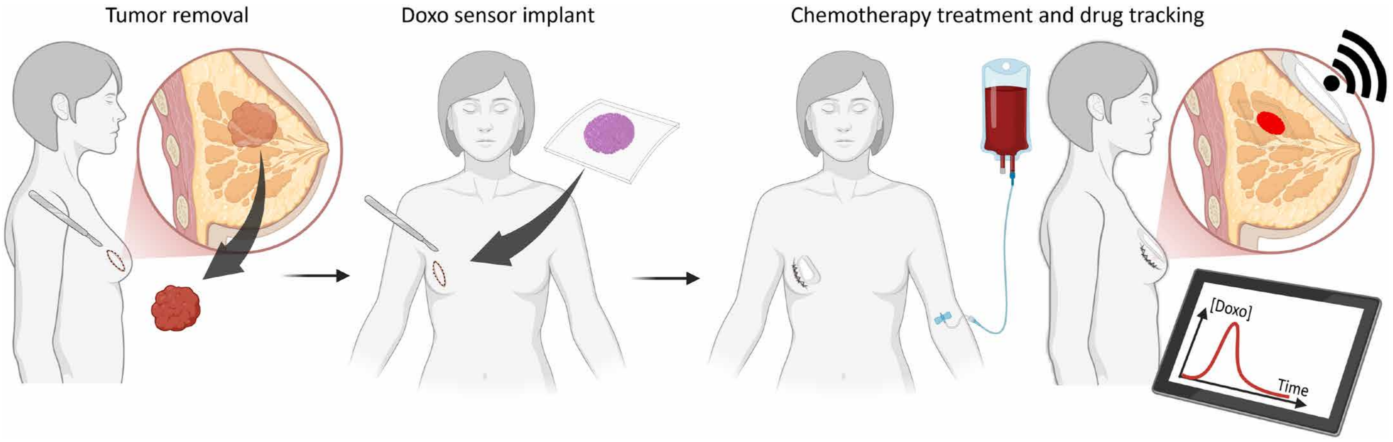

Fig. 1. Concept of in vivo monitoring of doxorubicin in tissue using a bioresorbable sensor coupled with a wearable readout patch. After primary tumor removal, the sensor is implanted under the skin, where it selectively detects doxorubicin (Doxo) levels in the tissue throughout chemotherapy treatment by enhancing the drug self-fluorescence. This enables real-time, noninvasive monitoring of doxorubicin concentration at the implantation site through the skin. The readout patch contains an electronic circuit designed to excite doxorubicin fluorescence and quantify its concentration in the tissue based on fluorescence intensity. The collected data are then transmitted in real time, wirelessly to a mobile device.

site for up to a few days following chemotherapy administration, whether during single-agent therapy regimens or continuous infusion protocols (*38*–*40*). The data, collected both in hospital settings and during patients' regular activities at home, complement systemic monitoring methods to guide dose adjustments once appropriate therapeutic indices are established, with the ultimate goal of preventing locoregional disease recurrence.

The biosensor (Fig. 2) consists of a nanostructured porous silica ($PSiO_2$) membrane with a diameter of 1 cm, a thickness of ~5 μm, and a pore size of ~30 nm in average, whose inner surface is functionalized with human serum albumin (HSA), known to bind doxorubicin in vivo (*41*) and serving as the bioreceptor. A thin (~100 μm) poly(D,L-lactic-*co*-glycolic acid) (PLGA) foil is used as the carrier of the biosensor. The use of a $PSiO_2$ membrane offers several advantages for the in vivo sensing of a fluorescent drug; namely, $PSiO_2$ can amplify the emission intensity of fluorescent molecules entrapped within it by a factor of 450, compared to a flat counterpart (*23*, *42*); it can reliably operate in vivo, enabling infiltration of target molecules within the pores while excluding unwanted analytes with size comparable or larger than the pores (*23*); in addition, $PSiO_2$ is bioresorbable and dissolves in vivo in safe by-products, namely, silicic acid, with a kinetics that can be tuned through oxidation (*22*, *43*–*45*). The biosensor configuration is unique in that it enables in vivo measurement of the drug concentrations by directly using the intrinsic fluorescence of doxorubicin enhanced through the porous silica scaffold, relying on the specific interaction between doxorubicin and the anchored HSA receptor.

Figure 2A shows the main preparation steps of the biosensor. A nanostructured PSi layer is prepared (fig. S1, A to C), peeled off the native silicon substrate, converted to $PSiO_2$ by thermal oxidation (fig. S1, D to F), and then transfer printed on the PLGA foil (Fig. 2A, steps 1 to 4). HSA is covalently linked to the inner surface of $PSiO_2$ through 3-aminopropyltriethoxysilane (APTES) and glutaraldehyde (GA). APTES is deposited from vapor phase to ensure a larger surface coverage and superior conformal coating (Fig. 2A, steps 5 to 7) (*46*, *47*). The functionalization protocol is optimized on flat SiO_2 and then transferred to the $PSiO_2$ membrane. Contact angle and roughness values measured on the flat SiO_2 after each step are consistent with those reported in the literature (*21*, *48*), validating the functionalization protocol (figs. S2 and S3). Consistently, the effective optical thickness (EOT) value measured on the $PSiO_2$ membrane increases after each step, confirming successful transfer of the functionalization protocol to the inner surface of the pores (fig. S4) (*49*). A picture of the biosensor is given in Fig. 2B.

We investigated the performance of the biosensor for doxorubicin detection in the range of 0.1 to 2 μg/ml in phosphate-buffered saline (PBS) and interstitial fluid (ISF) solutions at pH 7.4; the bare $PSiO_2$ membrane and flat SiO_2 sample were used as controls (Fig. 2, C to E). ISF is chosen to mimic in vivo application of the biosensor implanted in the subcutaneous tissue. The chosen range of concentrations reflects those expected in tissues after intravenous doxorubicin administration (*28*, *29*).

Figure 2C shows photoluminescence (PL) spectra acquired on the biosensor after incubation in ISF solution with increasing doxorubicin concentrations. The PL spectra exhibit a distinct peak at ~590 nm and a shoulder at ~550 nm, consistent with the expected doxorubicin emission (fig. S5) (*50*). The intensity of the PL emission steadily increases with the doxorubicin concentration, eventually reaching a steady-state value over time (fig. S6). Even at the lowest concentration tested, the signal is distinctly discernible above the noise floor ($N = 3\sigma \sim 180$ counts for both control samples and biosensor, where σ is the SD) with a good signal-to-noise ratio of ~13 at 590 nm. The biosensor exhibits a two orders of magnitude amplification (about 130x) of the doxorubicin emission compared to the flat SiO_2 control, confirming that the binding of doxorubicin predominantly occurs within the pores of the $PSiO_2$ membrane, as further corroborated by fluorescence images of its cross section (fig. S7). The amplification arises from the considerably larger effective surface of $PSiO_2$ (surface-to-volume ratio of ~550x compared to flat silica) (*23*), which facilitates the accumulation of a higher number of drug molecules per unit area. This amplification is crucial to enable measurements of the doxorubicin concentration through the skin based on the retrieved fluorescence intensity. Such measurements would be impractical otherwise, considering the inherently weak self-fluorescence of doxorubicin.

The stability of the doxorubicin emission within the biosensor was evaluated by monitoring the PL intensity at 590 nm in bare ISF, after incubation of the sensor in ISF solutions at various concentrations of doxorubicin (fig. S8). The PL intensity remains reasonably stable, with a maximum increase of ~10% observed at higher concentrations (1 and 2 μg/ml) assigned to a gradual redistribution of doxorubicin molecules bound to HSA probes over time, following the injection of bare ISF after incubation (fig. S8, A and B). This redistribution increases the distance between neighboring doxorubicin molecules, subsequently reducing PL self-quenching. No significant variation in the PL intensity over time is observed for the bare $PSiO_2$ membrane given the smaller number of doxorubicin molecules nonspecifically adsorbed on the silica surface, which is approximately one order of magnitude smaller than that in the biosensor (fig. S8, C and D).

The calibration curve of the biosensor in ISF achieved taking the PL intensity at 590 nm is presented in Fig. 2D. The biosensor demonstrates remarkable linearity across the tested range of doxorubicin concentrations, exhibiting excellent sample-to-sample reproducibility [coefficient of variation (CV%) = 8.6]. The biosensor sensitivity is 14 times higher than that of the bare $PSiO_2$ membrane, for which nonspecific adsorption of doxorubicin on the pore surface occurs. Such a remarkable improvement highlights the high specificity of the biosensor to doxorubicin. The biosensor achieves an LoD as low as ~3 ng/ml, which is below the smallest doxorubicin concentration of medical interest tested (i.e., 0.1 μg/ml) (Fig. 2E). We note that the flat SiO_2 substrate exhibits a PL emission that is comparable to the noise floor of the system across the whole tested range, regardless of the doxorubicin concentration. Control experiments carried out in PBS solutions of doxorubicin within the same concentration range show similar trends and performance to those observed in ISF, further confirming the robust operation of the biosensor in a complex biofluid environment (fig. S9, A to D).

Next, we assessed the performance of the biosensor in specific detection of doxorubicin in the presence of other drugs and HSA in the ISF solution to more closely mimic in vivo conditions. Cancer treatment often involves a combination of drugs, whose nature and concentration vary considerably based on the patient's therapeutic schedule. In this study, we considered a cocktail of four antineoplastic drugs commonly used for the treatment of breast cancer, namely, doxorubicin, paclitaxel (PA), cyclophosphamide (CY), and 5-fluorouracil (5-FU). Figure 2F shows the calibration curves of the biosensor in ISF solution spiked with either doxorubicin alone or

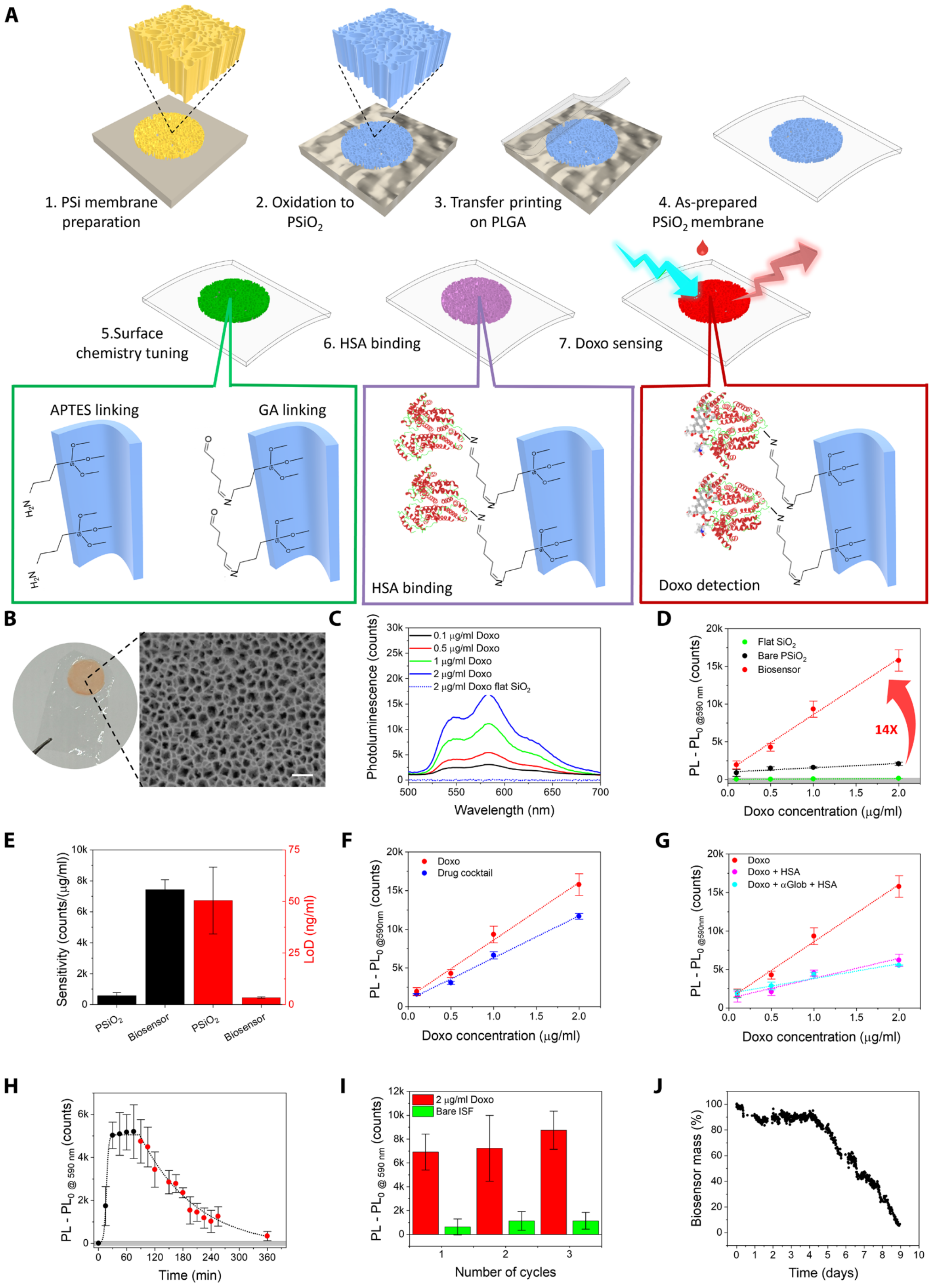

Fig. 2. Preparation and in vitro studies of the doxorubicin biosensor. (**A**) Sketch illustrating the main fabrication steps of the biosensor. (**B**) Picture of the biosensor (left) and top-view (right) of the nanostructured PSiO$_2$ membrane. Scale bar, 200 nm. (**C**) PL spectra of the biosensor after incubation in ISF solution with different doxorubicin concentrations. Blue dots indicate the PL emission recorded from the control sample (flat SiO$_2$). (**D**) Calibration curve of the biosensor (red dots, $n = 7$), i.e., PL at 590 nm versus doxorubicin concentration in ISF solution. Control samples include bare PSiO$_2$ membrane (black dots) and flat SiO$_2$ (green dots). Dashed lines represent linear fits to the calibration curves. PL$_0$ is recorded at 590 nm in bare ISF. (**E**) Sensitivity and LoD of the biosensor and control PSiO$_2$ sample in ISF solution. (**F**) Calibration curve of the biosensor in ISF solution spiked with doxorubicin only (red dots, $n = 7$) and with a cocktail of drugs, i.e., doxorubicin, PA, CY, and 5-FU. (**G**) Calibration curve of the biosensor in ISF solution containing doxorubicin only (red dots, $n = 7$), and with HSA (light blue dots) and α-globulin (αGlob; violet dots) in addition to doxorubicin. (**H**) PL at 590 nm over time of the biosensor upon exposure to doxorubicin (2 μg/ml) in ISF solution (black dots), followed by exposure to bare ISF (red dots), at 37°C. Dashed lines represent the best fit to experimental data. (**I**) PL at 590 nm of the biosensor after three incubation cycles with doxorubicin (2 μg/ml) in ISF (red bars) and in bare ISF (green bars). (**J**) Time-resolved mass variation of the biosensor in ISF solution at 37°C. Data in (D) to (I) are reported as the average value of three devices, with error bars representing the SD, if not stated otherwise. The gray area in (D) and (H) denotes the noise floor.

the drug cocktail, over the same concentration range of doxorubicin. The biosensor shows a linear increase in the emission intensity with doxorubicin concentration, regardless of the presence of other drugs. This indicates a remarkable level of specificity toward doxorubicin. The sensitivity reduces by 30% in the cocktail, consistently with the reduction of the emission intensity of doxorubicin in solutions containing other drugs, likely due to interactions with 5-FU (fig. S10) (*51*).

We then investigated doxorubicin detection in an ISF solution containing HSA at a concentration of 0.1 μM. It is worth noting that about 60% of circulating doxorubicin in the body binds to HSA, which is naturally present in human blood at a concentration of 0.66% (w/v), maintaining a state of thermodynamic equilibrium (*52*, *53*). Figure 2G (violet trace) shows that the biosensor maintains a linear dependence on doxorubicin concentration. As expected, a 65% reduction in the sensitivity value is observed, which is consistent with the percentage of doxorubicin known to bind to HSA in the solution. These results demonstrate the ability of the biosensor to measure the concentration of free doxorubicin (i.e., the fraction not bound to HSA in the solution), which is in its pharmacologically active state and of key importance for its role in medical therapy (*54*). Of note, the binding of doxorubicin to HSA does not affect the doxorubicin emission, as evidenced by control experiments conducted on ISF solution of doxorubicin with and without HSA (fig. S11A). The biosensor response remains unaffected even upon the addition of plasma proteins found in human blood, i.e., α-globulins, which do not bind doxorubicin (Fig. 2G, light blue trace, and fig. S11B).

The affinity constant value of HSA toward doxorubicin makes it an effective, reversible binding receptor (*55*), enabling the biosensor to track dynamic changes in doxorubicin concentration, both increasing and decreasing. The reversibility of this binding was validated in vitro under physiological conditions in a worst-case scenario using the highest tested drug concentration (2 μg/ml) in ISF solution containing HSA at physiological level. As shown in Fig. 2H, the biosensor response reaches saturation ~30 min after exposure to the doxorubicin solution. Upon removal of doxorubicin from the solution, the biosensor signal returns to baseline as the drug is released from HSA receptors, demonstrating a reversible binding behavior. This preserves the sensor functionality, enabling continuous monitoring of fluctuating drug levels (Fig. 2I).

The life span of the biosensor was assessed in an ISF solution under physiological conditions. The sensor remains stable for 4 days with a maximum variation of 4%. After this period, the silica scaffold begins dissolving with a mass rate of 16%/day and is fully dissolved after 9 days (Fig. 2J).

We next paired the biosensor with a compact wearable electronic circuit designed to be placed on the skin. This electronic patch serves the dual purpose of exciting and measuring the PL emission of doxorubicin captured by the implanted sensor, calculating the concentration of doxorubicin in the tissue and transmitting the real-time wireless data to a mobile device (Fig. 3A). A bottom view of the electronic patch is depicted in Fig. 3B and the block diagram in Fig. 3C. The circuit contains two light-emitting diodes (LEDs) with emission peaks at 450 and 455 nm, along with a photodiode (PD) with maximum sensitivity at 550 nm, to excite and collect the biosensor fluorescence, respectively. An adhesive filter film on the PD, with cutoff at ~520 nm, acts as a rejection filter for the LED light. A microcontroller (MC) drives the LEDs and reads the PD signal with a predefined timing sequence. The PD signal is then converted to a voltage value, digitized, and transmitted in real time to a mobile device (e.g., a tablet) for storage and presentation of the doxorubicin concentration using custom-designed application software.

Experiments with the electronic patch were conducted in an ISF solution at pH 7.4, with various doxorubicin concentrations. The biosensor was sandwiched between two synthetic skin flaps, with the patch placed on top of the skin (Fig. 3D). The electronic patch was programmed to interrogate the biosensor and transmit voltage data to the tablet every 10 s. Figure 3E shows the voltage values measured through skin and transmitted to the tablet by the electronic patch for different doxorubicin concentrations ranging from 0.1 to 2 μg/ml. The transmitted voltage remains stable over time and exhibits a steady increase with the doxorubicin concentration. The electronic patch reliably measures even the smallest doxorubicin concentration of 0.1 μg/ml. A linear relationship between voltage and doxorubicin concentration is established, with a sensitivity of 103 mV/(μg/ml), an LoD of 5 ng/ml, and a sample-to-sample reliability with CV% < 2.2% (Fig. 3F), which are consistent with the performance of the stand-alone biosensor.

We conducted additional experiments pairing the electronic reader with the biosensor placed under artificial skin of increasing thicknesses to simulate deeper sensor implantation. Figure 3G shows the output voltage of the reader at varying skin depths for a constant doxorubicin concentration of 2 μg/ml. The output voltage decreases linearly with the skin depth, a trend consistent with the attenuation of light within tissue due to scattering and absorption at shallow depth, as described by the modified Beer-Lambert law (*56*). Despite this attenuation, the experimental data demonstrate that the sensor can be successfully implanted at depths greater than 10 mm, with the doxorubicin signal reliably excited and retrieved above the noise floor with the electronic reader.

These results are of key importance as they validate the possibility of applying this technology in a clinical setting, using a wearable reader for the measurement of doxorubicin concentration through the skin.

We next proceeded with studies in an animal model to assess the sensing performance, as well as the biocompatibility and bioresorbability of the biosensor in vivo, following the protocol outlined in Fig. 4A. The biosensor was implanted in the subcutaneous tissue on the back of both adult male and female mice. A separate group of mice served as controls and received the same surgical procedures, except for the implantation of the sensor (hereinafter referred to as sham mice). Experimental procedures on mice were conducted in strict accordance with the ethical guidelines of the European Community (CEE Council 89 609; Italian DL 26/2014; authorization no. 979/2020 granted by the Italian Ministry of Health).

A first subgroup of mice was used to calibrate the biosensor in vivo. The calibration involved implanting biosensors that were preincubated in ISF solutions with known doxorubicin concentrations of 0.1, 0.5, and 2 μg/ml (hereinafter referred to as calibrators) and then measuring the fluorescence of the calibrators through the mouse skin (Fig. 4B). The calibrators were implanted in the mice with the $PSiO_2$ membrane facing the inner tissues (face-down orientation). Following the implantation, fluorescence images were acquired from these mice using an in vivo imaging system. Notice that fluorescence measurements of the calibrators in face-up and face-down configurations conducted before implantation with the same imaging system did not show any significant difference (fig. S12).

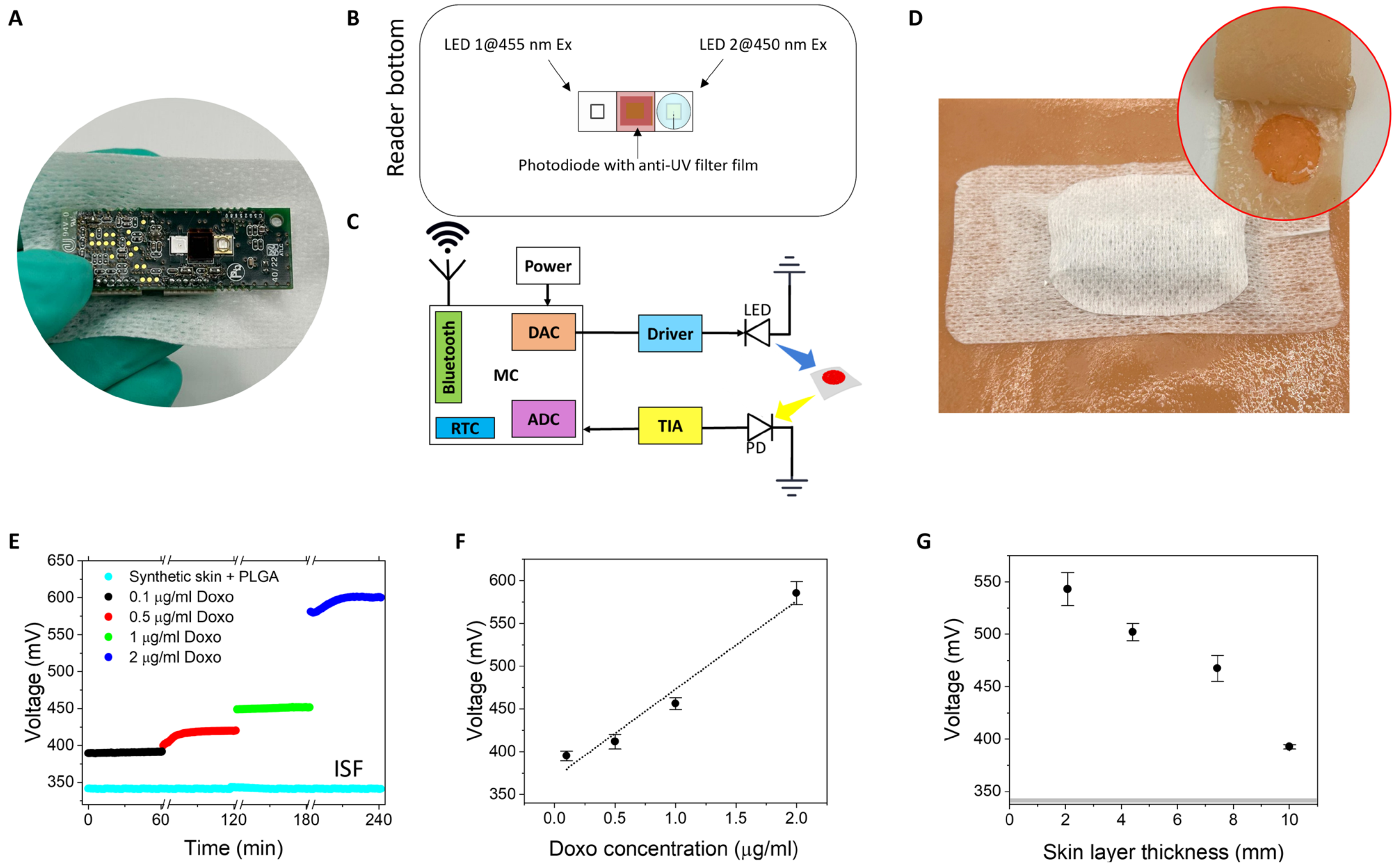

Fig. 3. Doxorubicin tracking using a readout electronic patch coupled to the biosensor. (**A**) Picture of the electronic patch. (**B**) Sketch of bottom side of the readout circuit in (A) highlighting the main components for excitation (LED) and collection (PD) of the doxorubicin emission. (**C**) Block diagram of the electronic reader for the doxorubicin biosensor. The reader includes a power source, an MC equipped with a digital-to-analog converter (DAC) for LED driving, and an analog-to-digital converter (ADC) for processing the output signal from a transimpedance amplifier (TIA) connected to the PD. Wireless communication (Bluetooth) and a real-time clock (RTC) enable remote, synchronized data transmission. (**D**) Picture of synthetic skin with the electronic patch positioned on top, placed in front of the biosensor that is sandwiched between two skin flaps (see inset). (**E**) Real-time voltage signal measured through synthetic skin using the electronic patch coupled with the biosensor, as shown in (C), and wirelessly transmitted to a tablet for different doxorubicin concentrations. The break symbol (//) on the *x* axes indicates 60-min incubation of the biosensor with doxorubicin. (**F**) Calibration curve (voltage versus doxorubicin concentration) of the biosensor measured with the electronic patch through synthetic skin [as shown in (D)] for different doxorubicin concentrations. (**G**) Output voltage of the electronic reader for a biosensor positioned at various depths in artificial skin, measured at a doxorubicin concentration of 2 μg/ml. The gray area represents the noise floor of the system. Data in (F) and (G) are reported as the average value measured over three devices, with error bars representing the SD.

Figure 4C shows representative fluorescence images from two animals implanted with calibrators at doxorubicin concentrations of 0.1 and 2 μg/ml. A distinct fluorescence emission at 620 nm is visible through the skin at the implantation sites of the calibrators for all tested doxorubicin concentrations. The intensity of fluorescence increases linearly with the concentration of doxorubicin in the calibrators. Figure 4D shows the average radiance value of the calibrators plotted against the concentration of doxorubicin. Any fluorescence contribution from the biosensor in the absence of doxorubicin was ruled out by in vitro experiments comparing the biosensor with calibrators (fig. S13), as well as by in vivo experiments on mice implanted with the biosensor prior to doxorubicin injection (fig. S14). In the latter, only tissue self-fluorescence was observed, similar to that in sham mice.

We used a second subgroup of mice to investigate the capability of the biosensor to detect doxorubicin concentration over time in vivo. In these mice, the biosensor was implanted in the subcutis 1 day before the intravenous administration of the drug (10 mg/kg) through the lateral caudal tail vein (Fig. 4E). Fluorescence images were acquired through the skin at different time points, namely, 1, 3, 24, and 48 hours after the intravenous injection of doxorubicin. The fluorescence signal acquired at the implantation site before doxorubicin injection served as reference. Figure 4F shows representative fluorescence images taken from one of the mice with the biosensor implanted, captured 3 and 48 hours after doxorubicin injection. The images clearly depict strong fluorescence at the implantation site after 3 hours, whereas no fluorescence is visible after 2 days as expected. Figure 4G shows the concentration-time curve of doxorubicin in the subcutis of animals ($n = 6$) up to 48 hours after injection. A distinct fluorescence emission is visible above the noise floor at the implantation site just 1 hour after intravenous injection. The emission intensity peaked after 3 hours, gradually decreasing over the next 48 hours to return to the baseline. No significant emission above the noise floor was measured after 48 hours postinjection. The doxorubicin

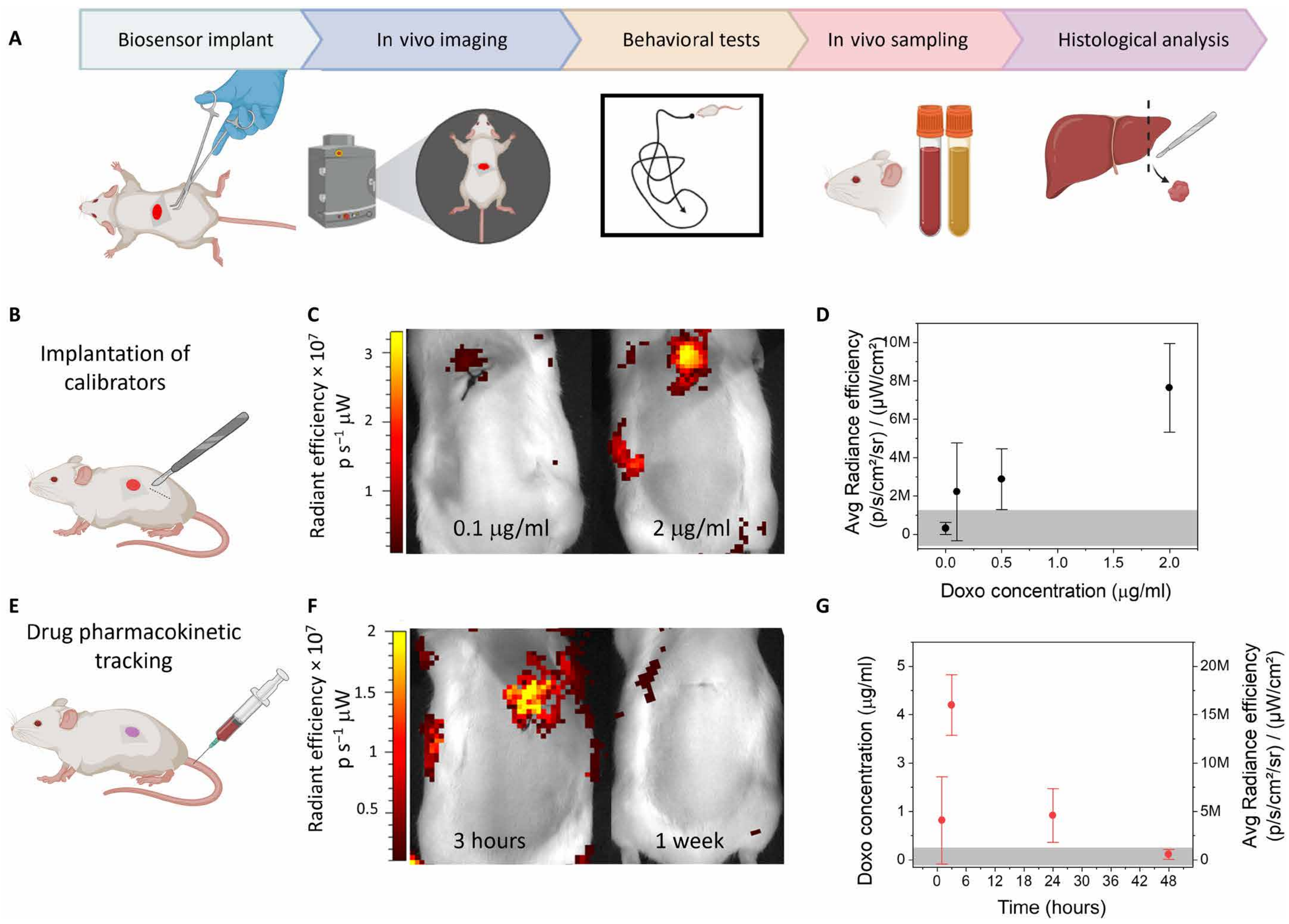

Fig. 4. In vivo tracking of the doxorubicin concentration through mouse skin using the biosensor. (**A**) Sketch illustrating the protocol used for in vivo experiments with the biosensor. (**B**) Sketch of a mouse implanted with the calibrators. (**C**) In vivo fluorescent images of mice implanted with calibrators loaded with doxorubicin (0.1 and 2 μg/ml). (**D**) In vivo calibration curve, namely, fluorescence intensity at the implantation site versus doxorubicin concentration, measured through skin on mice implanted with the calibrators ($n = 9$ mice). The gray area represents the noise floor, i.e., mean value ±3 times the SD of the fluorescence intensity measured on mice implanted with the biosensor without doxorubicin ($n = 9$ mice). (**E**) Sketch of a mouse implanted with the biosensor for in vivo drug pharmacokinetic tracking. (**F**) In vivo fluorescent images acquired on a mouse implanted with the biosensor 3 and 48 hours after doxorubicin (10 mg/kg) intravenous injection. (**G**) In vivo doxorubicin concentration over time following intravenous injection ($n = 6$ mice). The gray area represents the noise floor, i.e., mean value ±3 times the SD of the fluorescence intensity measured on mice implanted with the biosensor without doxorubicin ($n = 9$ mice). Data in (D) and (G) are shown as mean value with error bars representing the SD.

concentration in the tissue was calculated, leveraging the in vivo calibration of the biosensor reported in Fig. 4D to convert the average emission intensity into drug concentration. Notably, no fluorescence emission above the noise floor was observed at any of the time points in sham mice subjected to the same intravenous administration of doxorubicin. The pharmacokinetic parameters for doxorubicin at the implantation site are reported in Table 1. The maximum concentration ($C_{\max}$) reached aligns with in vitro concentrations responsible for antiproliferative activity (*57*), and the elimination half-life is comparable to previously reported ranges for similar intravenous administered doses in mice (*58*).

Biocompatibility was assessed in vivo in mice implanted with the biosensor and calibrators, with shame mice serving as controls, by means of behavioral scores recorded over 3 months after implantation at different time points, followed by biochemical and histological analyses after euthanasia. We monitored the weight of the animals throughout the entire experimental period, and no statistical difference between sham mice and those implanted with the sensors/calibrators was found (Fig. 5A and fig. S15A). The average weight variation from presurgery to each observational week (W1, 2, 4, 6, 8, 10, and 12) of each experimental group reported in Fig. 5A (see also fig. S15A) shows no significant alterations (see table S1 for statistical analysis). A body weight variation below 5% suggests the absence of critical suffering, according to the Federation of European Laboratory Animal Science Associations (FELASA) guidelines that define a body weight reduction of 20% or more as severe suffering (*59*). As for behavioral manifestations, locomotor activity and spontaneous exploration of the open-field arena were recorded before and at 1, 2, and 3 months after implantation (*60*, *61*). The total distance traveled and maximum speed (Fig. 5, B and C, and fig. S15, B and C), as well as the percentage of time spent in the center of the arena (Fig. 5D and fig. S15D), show no significant changes 1, 2, and 3 months after

Table 1. Pharmacokinetic parameters at the implantation site. Individual doxorubicin concentration versus time datasets were fitted according to an extravascular one-compartment model, by use of nonlinear least-squares regression analysis (MwPharm software, version 3.60; MediWare, Groningen, The Netherlands). The maximum plasma concentration (C_{max}) and time to reach C_{max} (T_{max}) were identified from the inspection of doxorubicin concentration–time plots. The elimination half-life ($t_{1/2}$) was obtained from the equation $t_{1/2} = 0.693/k$, where k is the slope of the exponent. The area under the curve was calculated by the trapezoidal method for the area from time 0 to the time of the last measurable concentration (48 hours) for doxorubicin. AUC, area under the curve; MRT, mean residence time.

Pharmacokinetic parameters	Mean	SD	Range
C_{max} (μg/ml)	4.02	0.78	2.94–4.70
T_{max} (hours)	3	0	3
$AUC_{0\text{-}48h}$ trapezoidal (hour·μg/ml)	71.71	13.25	57.96–88.80
Elimination half-life (hours)	8.62	3.80	5.02–13.75
MRT (hours)	12.43	5.48	7.41–19.84

implantation. We also monitored several parameters related to spontaneous behavior and mouse welfare indicators such as activity status, the presence/absence of tremor, lacrimation, eyelid closure, fur appearance, whisker movement, and defecation. The results demonstrate a lack of significant changes in these scores, suggesting the absence of systemic toxicity during the entire experimental period.

Three months after implantation, mice were euthanized. Blood was retro-orbitally collected, the skin above the implantation site was removed for histological analysis, and weight and macroscopic alterations in the liver, spleen, kidney, lung, heart, and brain were evaluated (Fig. 5, E and F). The analyses of the collected organs reveal no statistical difference in both parameters between the biosensor/calibrator-receiving mouse groups and sham mice (Fig. 5F and fig. S16A). Also, no significant changes in the serum alanine transaminase (ALT) levels, indicator of hepatic toxicity, are found among the three different mouse groups (Fig. 5G and fig. S16B). All these data are accompanied by the absence of significant alterations in the histological organization of the skin among the experimental mouse groups (Fig. 5, H to K, and fig. S16, C and D), further confirming the in situ biocompatibility of the biosensor and calibrators. The biocompatibility outcomes of the calibrators demonstrate that temporary accumulation of doxorubicin in the sensor does not induce toxicity in mice (tables S1 and S2). These comprehensive findings contribute to the overall assessment of the biosensor's safety and biocompatibility in the studied mouse model.

DISCUSSION

In this study, we investigate the potential of an implantable bioresorbable optical sensor designed to offer quantitative temporal monitoring of doxorubicin concentration in vivo at user-selectable positions, paving the way for the next phase in precision medicine.

This biosensor, with a thickness of just 5 μm and entirely composed of bioresorbable materials, demonstrates its efficacy through live animal testing, showcasing real-time monitoring of free doxorubicin at the subcutaneous level. The sensor features an LoD of 3 ng/ml and life span of 4 days. Leveraging the intrinsic fluorescence of doxorubicin as the output signal, this sensor amplifies the fluorescence intensity of a factor of 100, enabling its readout through the skin. By pairing the sensor with a reusable electronic patch placed on the skin's surface, real-time data collection and wireless transmission to a mobile device become feasible, offering unparalleled convenience and accessibility to drug pharmacokinetic data in tissue at the implantation site, even outside the hospital setting. Complete biodegradation was observed 3 months postimplantation, with no adverse effects detected in the implanted mice. Comprehensive biocompatibility assessments conducted over this 3-month period in live mice revealed no systemic toxicity indicators, biochemical abnormalities, or histological alterations, affirming the sensor's safety and compatibility.

In conclusion, our in vivo study successfully demonstrates the sensor's functionality, biocompatibility, bioresorbability, and ability to track doxorubicin concentrations with high spatial and temporal precision at the implantation site. Although the study was designed with specific constraints to ensure animal welfare and experimental feasibility, the results provide a strong foundation for future exploration of the sensor's applications in different anatomical sites and tumor microenvironments. These findings highlight the potential of the biosensor to improve chemotherapy monitoring in both presurgical and postsurgical settings, as well as in cases of inoperable metastatic tumors. Further studies will focus on expanding these applications and validating the sensor's clinical utility in more complex models.

Besides doxorubicin monitoring, the biocompatibility, bioresorbability, and in vivo functionality of the proposed sensing platform open the possibility of modifying the nanostructured porous silica pores and the bioreceptors within them to target other analytes and clinically relevant drugs for in vivo diagnostics.

MATERIALS AND METHODS

Materials and chemicals

Single-side polished silicon boron–doped wafers (p^{++} type) with a resistivity of 0.8 to 1.2 megohm·cm and crystallographic orientation <100> were purchased from Siltronix Silicon Technologies (France). Aqueous hydrofluoric acid (HF, 48%), sodium hydroxide (NaOH, 98%), aqueous hydrochloric acid (HCl, 37%), sodium acetate (CH_3COONa, 99%), APTES (99%), GA (50%), HSA, potassium chloride (KCl, 99%), sodium bicarbonate ($NaHCO_3$, 99.7%), sodium phosphate, (Na_2HPO_4, 99%), sodium phosphate monobasic monohydrate (PBS, 98%), sodium chloride (NaCl, 99%), chloroform ($CHCl_3$, >99%), PLGA (85:15 lactide:glycolide, M_w = 50,000 to 75,000), α-globulins

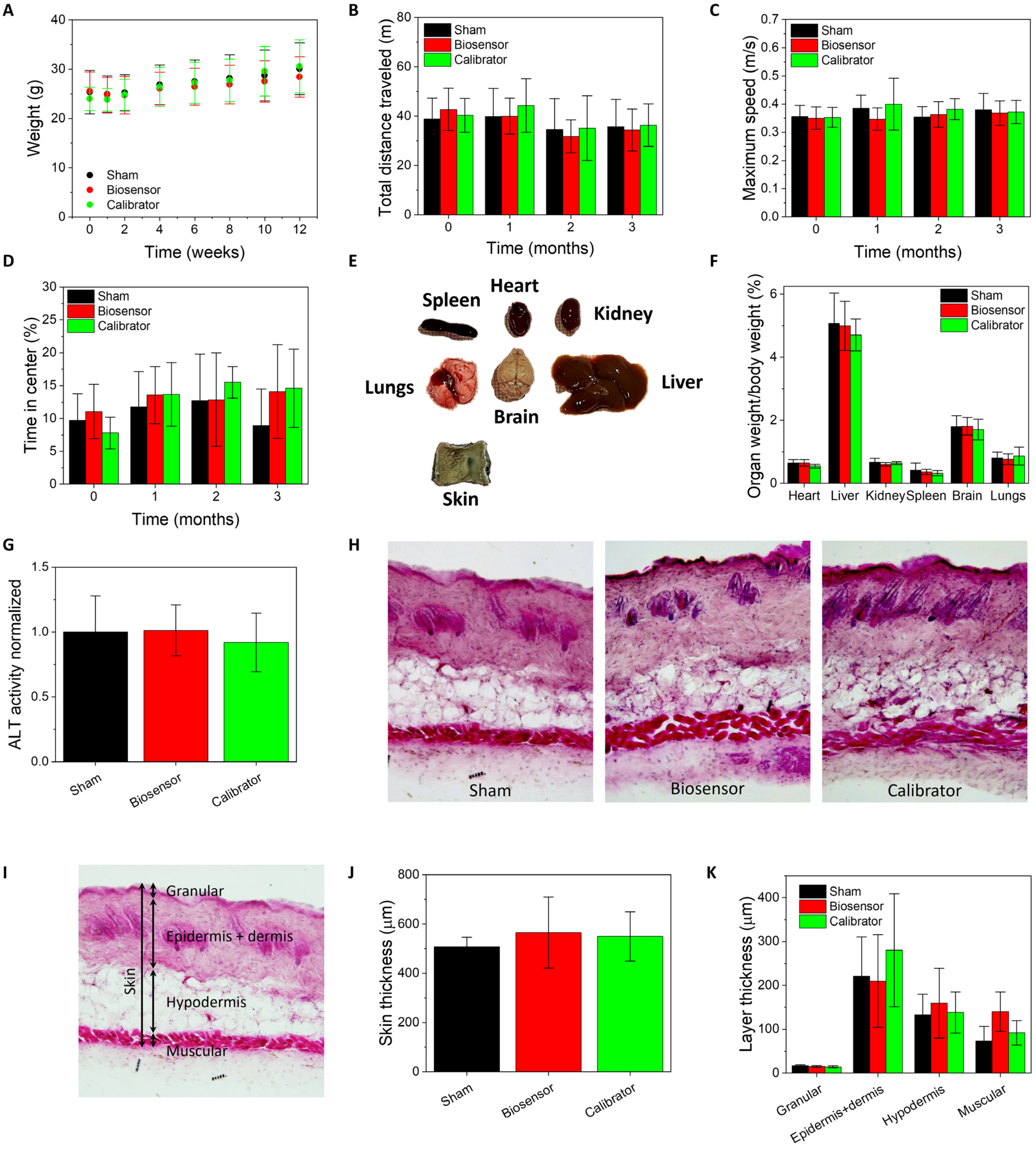

Fig. 5. In vivo biocompatibility study. (**A**) Weight over 3 months of sham mice ($n = 12$) and mice implanted with biosensors ($n = 11$) and calibrators ($n = 12$; four mice per dose). (**B** to **D**) Total distance traveled (B), maximum speed (C), and percentage (%) of time spent in the center (D) in the open-field arena by sham mice and mice implanted with the biosensor and the calibrators, measured at basal (0) and 1, 2, and 3 months after implant. (**E**) Images of harvested organs after 3 months from implantation: spleen, heart, kidney, lungs, brain, liver, and skin. (**F**) Weight of organs at euthanasia, normalized to mouse body weight, of mice in (A) after euthanasia at 3 months. (**G**) ALT assay in the serum collected from mice at euthanasia. (**H**) Representative images of skin of sham mice and mice implanted with biosensors and calibrators. (**I**) Skin histological image with different layers. (**J**) Skin thickness from histological images of sham mice ($n = 3$), biosensor ($n = 3$), and calibrators ($n = 12$). (**K**) Different layer (granular, epidermis + dermis, hypodermis, and muscular) thickness from histological images of sham mice ($n = 3$), biosensor ($n = 3$), and calibrators ($n = 12$). Data in (A) to (D), (F), (H), (J), and (K) are shown as mean value with error bars representing the SD by repeated two-way ANOVA or one-way ANOVA as appropriate.

Cohn (fraction IV-4) human, ProClin 150, paraformaldehyde (4%), and ALT activity assay were purchased from Merck–Sigma-Aldrich (Germany). Absolute ethanol (EtOH, 99.9%), isopropyl alcohol (99.5%), diethyl ether (Et_2O, >99%), sulfuric acid (H_2SO_4, 96%), hydrogen peroxide (H_2O_2, 30%), and hematoxylin and eosin were purchased from Carlo Erba Reagents (Italy). Aqueous solutions were prepared using deionized water (DIW; 15 megohm·cm) filtered by Elix (Merck Millipore, Germany). Skin toughness synthetic human tissues (2 N) were purchased from SynDaver (USA). Polydimethylsiloxane (PDMS; Sylgard 184) base and thermal curing agent were purchased from Cecchi S.r.l. (Italy). Doxorubicin (2 mg/ml), PA (6 mg/ml), CY (20 mg/ml), and 5-FU (50 mg/ml), Betadine, and Neuflan were purchased from the pharmacy of the hospital of Modena (Italy). Isoflurane (Vetflurane, 1000 mg/g) was purchased from Virbac (Italy). Histo-mount was purchased from HIsto-Lab (Italy). Sucrose (99%) was purchased from Thermo Fisher Scientific (USA). All buffers were prepared in DIW and pH adjusted with NaOH (5 M) and HCl (5.4 M) aqueous solution.

Preparation of the $PSiO_2$ layer on a silicon substrate

A custom-made Teflon cell equipped with a platinum wire and an aluminum plate operating as a cathode and anode, respectively, was used to perform the electrochemical etching of a silicon substrate (1.5 cm by 1.5 cm) over a circular area of 0.567 cm^2. A source measurement unit (SMU; Keithley 2602A) was used to set the etching current and measure the voltage drop between the anode and cathode. Initially, a sacrificial PSi layer was prepared using a solution of HF:EtOH (3:1, v/v) and an etching current density of 350 mA cm^{-2} for 20 s. After rinsing the sample in EtOH for 120 s to remove residual HF, the as-prepared PSi layer was fully dissolved upon immersion in a NaOH (1 M):EtOH (9:1, v/v) solution for 120 s, achieving a nanostructured templating surface that prevented formation of a parasitic layer. The resulting sample was rinsed in DIW and EtOH and used to etch a sensing PSi layer at 350 mA cm^{-2} for 40 s, resulting in a thickness of ~4.3 μm and a porosity of ~77%. The sample was then rinsed in EtOH for 120 s and Et_2O for 60 s to obtain a crack-free PSi layer. Eventually, PSi layers were thermally oxidized to $PSiO_2$ in a muffle furnace (ZB/1, ASAL, Italy) at 1000°C for 5 min (*23*, *42*, *62*).

The porosity value was chosen as the highest achievable during the PSi membrane preparation while ensuring its mechanical stability, specifically 77% (*63*). This ensures the largest possible pore diameter after oxidation, thereby enhancing molecular diffusion within the pores during functionalization and sensing experiments. Notably, the porosity reduces from 77 to 55% after oxidation, as expected, due to volume expansion of the silicon skeleton when converted to SiO_2.

Preparation of a PLGA foil

A polymer solution was prepared by dissolving 0.2 g of PLGA pellets in 10 ml of chloroform at room temperature (RT). The solution was gently stirred for 6 hours under a glass cover to prevent solvent evaporation. The prepolymer was then dropped onto a glass petri dish (9 cm in diameter) closed with a glass cover and left overnight in an air-saturated environment with chloroform vapors. The PLGA film was then manually peeled off the petri dish, with immersion in DIW aiding in its detachment. Last, the PLGA film was gently dried in a ventilated oven (G-Therm 035, Fratelli Galli, Italy) at 30°C for 5 min (*23*).

Preparation of the $PSiO_2$ membrane on a PLGA foil

A custom-made Teflon cell equipped with a platinum wire and an aluminum plate operating as a cathode and anode, respectively, was used to perform the electrochemical etching of a silicon substrate (1.5 cm by 1.5 cm) over a circular area of 0.567 cm^2. An SMU (Keithley 2602A) was used to set the etching current and measure the voltage drop between the anode and cathode. Initially, a sacrificial PSi layer was prepared using a solution of HF:EtOH (3:1, v/v) and an etching current density of 350 mA cm^{-2} for 20 s. After rinsing the sample in EtOH for 120 s to remove residual HF, the as-prepared PSi layer was fully dissolved upon immersion in a NaOH (1 M):EtOH (9:1, v/v) solution for 120 s, achieving a nanostructured templating surface that prevented the formation of a parasitic layer. The sample was rinsed in DIW and EtOH and then etched with a current density of 20 mA cm^{-2} for 150 s to achieve a barrier PSi layer with a thickness of ~1 μm and a porosity of ~62%, which was functional to prevent polymer diffusion into the pores during the transfer printing process. The sample was rinsed in EtOH for 120 s to remove residual HF, and then a sensing PSi layer with a thickness of ~4.3 μm and a porosity of ~77% was etched at 350 mA cm^{-2} for 40 s underneath the barrier layer. The sample was rinsed in EtOH for 120 s and Et_2O for 120 s to obtain a crack-free PSi layer.

We then scratched a circular contour into the PSi surface with a diamond tip to separate the PSi from the surrounding native Si substrate. The PSi layer was then fully detached from the native Si substrate, achieving a PSi freestanding membrane through an electropolishing step performed in the Teflon cell at an etching current density of 800 mA cm^{-2} for 0.1 s. An etching solution consisting of HF:EtOH (1:1, v/v) with reduced HF concentration was used to facilitate the electropolishing step.

The PSi membrane was rinsed in EtOH and Et_2O and then sandwiched between two nonpolished silicon dices. The PSi membrane was eventually converted into porous silica ($PSiO_2$) through a thermal oxidation step conducted at 1000°C for 5 min in a muffle furnace (ZB/1, ASAL, Italy). Once oxidized, the topmost silicon dice was lifted off and a PLGA foil (3 cm by 2 cm, thickness of 100 μm) was placed on top of the as-prepared $PSiO_2$ membrane. The PLGA-$PSiO_2$-Si assembly was heated at 100°C for 60 s on a hot plate (ARE 230V, Velp Scientifica, Italy) and then rinsed with DIW to lift off the PLGA-$PSiO_2$ from the hosting Si substrate. Last, the PLGA-$PSiO_2$ was gently dried at 30°C for 5 min in a ventilated oven (G-Therm 035, Fratelli Galli, Italy) (*23*, *42*, *62*).

HSA anchoring

Immobilization of the bioreceptor for doxorubicin onto $PSiO_2$ membranes embedded in either the native Si substrate or transfer printed on a PLGA foil involved the covalent anchoring of HSA to the inner $PSiO_2$ surface using a suitable linker. First, the $PSiO_2$ membrane was functionalized with APTES. Specifically, the $PSiO_2$ surface was chemically activated by immersion in a solution of H_2SO_4:H_2O_2 (4:1, v/v) for 1 hour, followed by rinsing in DIW for 5 min. The membrane was then exposed for 30 min to vapors of an APTES solution in toluene (10%, v/v) at 120°C (*46*) and eventually immersed in a 5% (v/v) GA solution in 10 mM PBS at pH 7.4 for 2 hours, followed by rinsing in DIW for 5 min. To anchor the protein, a solution of HSA (1 mg/ml) in 10 mM PBS at pH 7.4 was drop cast (100 μl) onto the GA-functionalized $PSiO_2$ membrane and left for 2 hours at RT and then rinsed in DIW for 5 min. After each step, the reflectance spectrum of the $PSiO_2$ membrane was acquired as detailed in the section Optical reflection spectroscopy.

Morphological characterization

Top-view and cross-sectional morphological characterization of PSi and $PSiO_2$ membranes were carried out using a scanning electron microscope (FEG-SEM, Zeiss SUPRA) with a 10-kV acceleration voltage at various magnifications. The distribution of the pore diameters was obtained from the analysis of top-view SEM image with Gwyddion software.

Cross section of the biosensor on the native Si substrate was examined after incubation with doxorubicin (2 μg/ml) in ISF solution using an optical microscope (Leica DM2500 M) in both bright-field and fluorescence modes. Fluorescence imaging was performed with a blue laser diode (λ_{ex} = 450 nm, 4.5 mW, CPS450, Thorlabs, USA) as the excitation source.

Optical reflection spectroscopy

Reflectance spectra of the PSi layer and bare $PSiO_2$ membranes, as well as those of the biosensor were measured in the wavelength range of 400 to 1000 nm at normal incidence in air. Light emitted by a deuterium and tungsten halogen lamps (DH-2000-BAL, OceanOptics, USA) was orthogonally shed through one arm of a bifurcated fiber-optic probe (QR200-7-SR, OceanOptics, USA) onto the sample surface. The reflected light was collected through the other arm of the fiber probe coupled to an ultraviolet-visible (UV-VIS) spectrometer (USB2000+ UV-VIS, Ocean Optics, USA). Reflectance spectra were recorded with an integration time of 2 ms and a spectral resolution of 0.35 nm. The line shape of the light source spectrum was corrected through normalization with respect to the reflectance spectrum of a silver mirror (PF10-03P01-Ø1, Thorlabs, USA). Undesired contributes due to the environmental light were also subtracted.

Porosity, thickness, and EOT of the PSi and $PSiO_2$ membranes and biosensors were evaluated by best fitting of the reflectance spectra using a Fabry-Pérot interferometer model.

Contact angle measurement

The wetting behavior of flat silica (SiO_2) surfaces was studied after each functionalization step through contact angle goniometry. Specifically, 10 μl of DIW was deposited on top of the sample under investigation and an optical image of the droplet profile was recorded using a complementary metal-oxide semiconductor camera (DCC1545M, Thorlabs). Contact angle values were extracted through the optical images by using the contact angle plug-in of ImageJ. To ensure good reliability, three measurements were performed for each functionalization step.

AFM analysis

Morphological surface characterization of functionalized silica (SiO_2) surfaces was performed using atomic force microscopy (AFM; DIMENSION edge, Bruker, Italy) equipped with an ASYLEC-01-R2 tip (silicon tip Ti/Ir coated, $f0$ = 75 kHz, k = 2.8 N/m) and operating in tapping mode. Size, distribution, and surface coverage of molecules on the silica surface were evaluated by postprocessing AFM images in Gwyddion. The surface roughness of the samples was measured as the root mean square value of the AFM height maps over an area of 1 μm by 1 μm. Possible tilts in the AFM images were removed using Nanoscope Analysis software.

Preparation of synthetic ISF

Synthetic ISF solutions consisted of mixtures of NaCl (107.7 mM), KCl (3.48 mM), $CaCl_2$ (1.53 mM), $MgSO_4$ (0.69 mM), $NaHCO_3$ (26.2 mM), NaH_2PO_4 (1.67 mM), Na gluconate (9.64 mM), glucose (5.55 mM), and sucrose (7.6 mM) (*64*).

Synthetic ISF solutions containing proteins (11 g/liter, in total) were prepared by dissolving HSA (1 μM) and α-globulins in a ratio of 60:40 in PBS buffer, the latter containing ProClin 150 (6 μg/ml) used as a preservative and disinfectant agent (*65*).

Preparation of drug cocktail solution in ISF

Drug cocktail solution in ISF buffer was prepared with PA (0.5 μg/ml), CY (1 μg/ml), 5-FU (1 μg/ml), and doxorubicin at concentrations of 0.1, 0.5, 1, and 2 μg/ml.

In vitro incubation with doxorubicin solutions

Control devices and the biosensor were incubated in 6 ml of either PBS (10 mM + 100 mM NaCl) or ISF solutions, with and without HSA, of doxorubicin at concentrations of 0.1, 0.5, 1, and 2 μg/ml. The incubation was performed in a standard polystyrene petri dish (3.5 cm in diameter) for 60 min at RT, a duration selected based on kinetic binding experiments.

To determine the optimal incubation time, sensors were incubated at 15-min intervals up to 90 min, and the PL signal of three independent sensors was measured at each time point. The sensors were incubated at 15-min intervals up to 90 min, and the PL signal of three independent sensors was measured at each time point. After incubation at a given doxorubicin concentration, samples were rinsed in DIW for 30 s and dried under a gentle nitrogen flux.

PL of doxorubicin solutions

Doxorubicin solutions (600 μl) at concentrations of 0.1, 0.5, 1, and 2 μg/ml were prepared in different buffers (i.e., PBS buffer and ISF with or without HSA) and dropped into a quartz μ-fluorescence cuvette (CV10Q700, 700-μl volume, Thorlabs, USA) for PL spectra measurement. The excitation source was a green laser diode (λ_{ex} = 520 nm, 4.5 mW, Thorlabs, USA) emitting a collimated elliptical beam (beam size: 4.6 mm by 1.7 mm). The beam was directed toward the cuvette, and the emitted light was collected through an optical fiber (QR600-7-VIS-NIR, OceanOptics, USA) orthogonal to the direction of the excitation. The optical fiber guided the emitted light to a UV-VIS spectrometer (HR4000CG-UV-NIR, Ocean Optics, USA). PL spectra were recorded with an integration time of 1 s and a spectral resolution of 0.97 nm.

PL spectroscopy of control devices and biosensor

PL spectra of control devices and the biosensor on the PLGA foil were collected in the wavelength range of 400 to 1000 nm in air, using a blue laser diode (λ_{ex} = 450 nm, 4.5 mW, CPS450, Thorlabs, USA) emitting a collimated elliptical beam (3.2 mm by 1.0 mm in size). The beam impinged the bottom surface of the PLGA foil with an angle of ~30°, whereas the emitted light was collected through a lens-terminated optical fiber (CVH100-COL, Thorlabs, USA), the latter connected to a UV-VIS spectrometer (USB2000+ UV-VIS, Ocean Optics, USA). The PL spectra were recorded with an integration time of 2 s and a spectral resolution of 0.35 nm.

PL spectra of control devices and the biosensor on the native Si substrate were acquired in the wavelength range of 400 to 1000 nm in air. The excitation source was a green laser diode (λ_{ex} = 520 nm, 4.5 mW, CPS520, Thorlabs, USA) emitting a collimated elliptical beam (4.6 mm by 1.7 mm in size). The beam impinged onto the topmost surface of the $PSiO_2$ membrane with an angle of ~30°, whereas the emitted light was collected through one arm of a bifurcated fiber-optic probe (QR200-7-SR, OceanOptics, USA) coupled to a UV-VIS spectrometer (USB2000+ UV-VIS, Ocean Optics, USA). The PL spectra were recorded with an integration time of 2 s and a spectral resolution of 0.35 nm.

The calibration curve was obtained by plotting the PL peak intensity at 590 nm against the doxorubicin concentration. The sensitivity (S) was determined as the slope of the linear fit to the experimental data points. The LoD was calculated based on the SD of the background noise and the sensitivity using the following formula

$$\mathrm{LoD} = \frac{3\sigma_n}{S}$$

where σ_n is the SD of the PL signal acquired before doxorubicin incubation, and S is the sensitivity.

In vitro kinetics of doxorubicin interaction with the biosensor

The biosensor was incubated with ISF solutions containing HSA at doxorubicin concentration of 2 μg/ml at 37°C, and the PL signal was measured at 15-min intervals up to 90 min to assess binding saturation as described in the section PL spectroscopy of control devices and biosensor. Following stabilization of the signal, the sensors were immersed in bare ISF (without doxorubicin) and the PL signal was recorded every 15 min to monitor the release kinetics of doxorubicin. The binding process was considered stable when the PL signal reached 90% of its maximum value. This time was calculated by fitting the experimental data to the following logistic equation

$$y = \frac{a}{\left[1 + e^{-k1(x - xc)}\right]}$$

where a, $k1$, and xc are fitting constants.

Doxorubicin release was modeled using an exponential decay function

$$y = be^{-\frac{x}{k2}} + y0$$

where b, $k2$, and $y0$ are fitting constants.

The time for complete release was determined through best fitting of the experimental data to the model, providing a quantitative assessment of the reversibility of the HSA-doxorubicin interaction.

Biosensor response to repeated doxorubicin concentrations

The biosensor was exposed to repeated cycles of doxorubicin incubation to evaluate its response consistency and reversibility. The cycle was repeated three times, with doxorubicin concentrations alternating between a fixed value and zero. Specifically, the biosensor was incubated in ISF solution containing HSA at 0.1 μg/ml and doxorubicin at 2 μg/ml at 37°C, and the PL signal was measured after 30 min as described in the section PL spectroscopy of control devices and biosensor. The biosensors were then immersed in bare ISF without doxorubicin, and the PL signal was recorded after 300 min. The cycle was repeated three times. PL intensity values at 590 nm were taken as the sensor response.

Real-time sensing of doxorubicin

Control devices and the biosensor on the native Si substrate were incubated with doxorubicin solution, as described in the section In vitro incubation with doxorubicin solutions. Following the incubation, the samples were immersed in ISF solution and PL spectra were acquired every 5 for 60 min, as detailed in the section PL spectroscopy of control devices and biosensor. Specifically, the samples were secured within a custom PDMS o-ring [base:curing agent, 10:1 (w/w), curing temperature of 90°C, and curing time of 1 hour] with a diameter of 7 mm, filled with 300 μl of ISF, and covered with a microscopy glass slide to prevent liquid evaporation over time.

Doxorubicin sensing with a wearable electronic circuit

The wearable electronic circuit for doxorubicin sensing comprised two blue LEDs (GD CSSPM1, OSRAM, Germany, emitting at a peak wavelength of 455 and 450 nm, with a forward current of 100 mA) and a PD (SFH 2270R, OSRAM, Germany, peak sensitivity at 560 nm, operated at −1-V bias voltage). The PD was equipped with an in-line long-pass filter tape (Lithoprotect YSA520, durXtreme GmbH, Germany, cutoff wavelength of ~520 nm) to filter out the excitation light. The LEDs were used to provide excitation light, and the PD was used to collect the sensor fluorescence. Two batteries of ±3 V were used as a power supply of the circuit. For wireless data transfer, the circuit was equipped with an MC (STM32WB5MMG, STMicroelectronics) that performed analog-to-digital conversion and logic computations, along with a Bluetooth module (802.15.4). The electronic reader has a compact size of 1.5 cm by 4.5 cm and is fully programmable via an app running on the Android platform. The app also enables real-time data retrieval from the reader and displays the output on a mobile device.

For sensing experiments, the biosensor was incubated in ISF solutions containing specific concentrations of doxorubicin as described in the section In vitro incubation with doxorubicin solutions and then sandwiched between two flaps of a synthetic skin, which had been preconditioned in ISF solution (pH 7.4) overnight. The wearable circuit was placed on top of the synthetic skin, in the proximity of the sensor. The sensor's PL was then excited and collected every 10 s using the LED/PD pair, and the reader's output voltage transmitted in real time to a mobile device.

For evaluation of the maximum depth at which the biosensor can be effectively excited and read by the electronic reader, the biosensor was incubated with an ISF solution of doxorubicin at 2 μg/ml, as described in the section In vitro incubation with doxorubicin solutions, and then placed beneath an increasing number (from 1 to 4) of synthetic skin flaps, which had been preconditioned in ISF solution (pH 7.4) overnight. The wearable circuit was placed on top of the synthetic skin, in the proximity of the sensor and the sensor's PL was excited/collected every minute, and the reader's output voltage was transmitted in real time to a mobile device.

In vitro dissolution kinetics of the biosensor

Dissolution of the biosensor on the native Si substrate was carried out in a flow cell to simulate physiological ISF flow. The sample was secured into a flow cell system placed in a ventilated oven at 37°C (G-Therm 035, Fratelli Galli, Italy). A syringe pump (Nexus 3000, Chemyx Inc., USA) was used to inject an ISF solution at pH 7.4 at a flow rate of 100 μl min^{-1} for 4 min to fill up the system. The rate of injection of the ISF solution was then reduced to 0.7 μl min^{-1}, and reflectance spectra were acquired as detailed in the section Optical reflection spectroscopy every 5 min. The peak amplitude and position of the fast Fourier transform spectrum were used to calculate the mass dissolution of the biosensor.

In vivo experiments

Animals

For in vivo studies, 3-month-old C57BL6/J and CD1 male and female mice ($n = 50$) were used; progenitors were purchased from Charles River (Calco-Milan, Italy). Mice were housed in a pathogen free facility and kept in conditioned rooms with stable temperature (21° ± 0.5°C) and humidity (60%), on a 12-hour/12-hour light/dark cycle with food and water available ad libitum. Mice were maintained on a chlorophyll-free diet to reduce skin-autofluorescence interference during in vivo imaging system (IVIS) imaging (*66*). All animal procedures were approved by the Committee on Animal Health and Care of the University of Modena and Reggio Emilia and conducted in accordance with National Institutes of Health guidelines (*67*). Both strains were used for biocompatibility studies, as already reported in the literature (*68*, *69*). All efforts were made to minimize animal suffering and to reduce the number of animals used in this study.

Sensor and calibrator implantation procedure

Under deep anesthesia with inhaled isoflurane, mice were prepared for surgery by shaving their backs to minimize background fluorescence. The upper back skin was disinfected with Betadine, lifted, and incised, and a subcutaneous pouch of 1.5 cm by 1.5 cm was created for the insertion of the biosensor or calibrator. The incision was sutured by applying a surgical stitch and treated with Neuflan gel (0.5 g of neomycin/0.025 g of fluocinolone acetonide/2.5 g of lidocaine) to minimize local postoperative pain and the risk of infections.

Two separate cohorts of animals were used for biocompatibility and functionality/sensing studies.

For biocompatibility studies, 12 sham mice, 11 biosensor-implanted mice, and 12 calibrator-implanted mice (three mice for each dose of doxorubicin, namely, 0.1, 0.5, 1, and 2 μg/ml) were subjected to a 3-month-long observational period; after that, mice were euthanized to perform ex vivo toxicity evaluations such as biochemical and histological analyses.

For the functionality/sensing study, six mice were subjected to an intravenous injection of doxorubicin (10 mg/kg) after biosensor implantation and compared with calibrator-implanted mice (four mice per dose of doxorubicin, namely, 0.1, 0.5, and 2 μg/ml).

Intravenous injection of doxorubicin and IVIS imaging

Twenty-four hours after implantation, biosensor-implanted mice were placed in a recovery room at 37°C for 15 min to elicit vasodilation and received a single injection of doxorubicin (10 mg/kg) in the lateral caudal tail veins while restrained. Doxorubicin fluorescence of biosensor-implanted mice after intravenous injection was assessed, under anesthesia with isoflurane, using the IVIS (Lumina III, PerkinElmer) imaging system before and 1, 3, 24, and 48 hours after implantation. Doxorubicin fluorescence of calibrator-implanted mice was assessed, under anesthesia with isoflurane, using the IVIS (Lumina III, PerkinElmer) imaging system before implantation. A specific doxorubicin filter was used for excitation (from 480 to 560 nm with a 20-nm step size for excitation and 620 nm for collection), and average radiant efficiency (Avg Radiance) was calculated after autofluorescence subtraction. The region of interest over which radiant efficiency was measured was kept constant over different experiments on the same and different animals.

In vivo toxicity evaluation: Behavioral analysis

A SHIRPA modified test was used to monitor general health status including weight gain, appearance, locomotor activity, spontaneous behavior, and reflex reactions (*70*, *71*). Specifically, parameters such as activity status, tremor, lacrimation, eyelid closure, fur appearance, whisker movement, and defecation were scored. To evaluate the locomotor activity and the spontaneous exploration (as index of anxiety), an open-field test was conducted before implantation (baseline) and once a month for 3 months after implantation (*60*, *61*). Briefly, mice were placed in in the center of an open wooden chamber (50 cm by 50 cm by 40 cm) with dark walls and allowed to explore freely for 10 min. The open space was virtually subdivided into three zones, namely, periphery (within 10 cm of the walls), center (the rest of the arena), and corners for assessment of anxiety-influenced percentage of exploration time. Traveled distance, maximum speed, and the percentage (%) of time spent in each zone were automatically recorded and analyzed using the ANY-maze Video Tracking system (Stoelting). The apparatus was thoroughly wiped with 70% EtOH after each test to avoid olfactory cues. All behavioral and phenotypical observations/scores were performed by an operator unaware of the experimental group to avoid bias.

Euthanasia and organ collection

Animals in the biocompatibility study were euthanized 3 months after sensor implantation. Blood was collected via the retro-orbital route using a glass capillary, let coagulate at RT for 30 min, and then centrifuged at 1200 rcf for 15 min; serum was isolated and stored at −20°C until use. In addition, peripheral organs such as the liver, spleen, kidney, heart, lung, brain, and skin were collected, weighted, and submerged in physiological solution (0.9% NaCl) until IVIS fluorescence detection; then, organs were immerged and postfixed in 4% paraformaldehyde for 48 hours at 4°C and rinsed in a cryoprotective solution of 20% sucrose dissolved in PBS buffer for ~48 hours and then in a 30% sucrose dissolved in PBS buffer for 72 hours. All organs were frozen using dry ice and stored at −80°C for following histological analyses.

Ex vivo toxicity evaluation

Histological analysis of skin

A transversal 40-μm-thick section of skin series was cut with a cryostat (Leica CM1520), mounted on glass slides, and stored at −20°C. Slides were air dried at RT for 4 hours prior to hematoxylin and eosin histological staining and performed according to validated protocols (*23*). Histological images were captured using an optical microscope (Nikon Eclipse Ci) with a 10X objective and a Nikon DS-Fi3 camera. The thickness of different skin layers (granular layer, epidermis and dermis, hypodermis, and muscular cell layer) was measured through length tool measurement in Nikon NIS-Elements D software (5.21.00v).

Hepatic toxicity evaluation

Serum ALT activity (U/liter), an indicator of hepatic toxicity, was evaluated using ALT activity assay according to the manufacturer's instructions (MAK052, Sigma-Aldrich). Briefly, ALT activity was evaluated through an enzymatic colorimetric assay, using 20 μl of serum per sample, with absorbance reading at 570 nm (Multiskan FC, Thermo Fisher Scientific) and calculated using a linear regression method, with a pyruvate standard curve.

Statistical analysis

In vitro data are presented as means with SD values. All the data referring to more than three devices are presented, indicating the sample size (n).

As concerns in vivo study, differences between experimental groups were evaluated by one-way analysis of variance (ANOVA) or two-way repeated measures ANOVA as appropriate; sex was used as covariate. Significance was determined at $P < 0.05$, denoted as $*P < 0.05$, $**P < 0.01$, and $***P < 0.001$. The statistical package SPSS (version 26) was used.

Supplementary Materials

This PDF file includes:
Figs. S1 to S16
Tables S1 and S2

REFERENCES AND NOTES

1. U. Anand, A. Dey, A. K. S. Chandel, R. Sanyal, A. Mishra, D. K. Pandey, V. De Falco, A. Upadhyay, R. Kandimalla, A. Chaudhary, J. K. Dhanjal, S. Dewanjee, J. Vallamkondu, J. M. Pérez de la Lastra, Cancer chemotherapy and beyond: Current status, drug candidates, associated risks and progress in targeted therapeutics. *Genes Dis.* **10**, 1367–1401 (2023).
2. D. M. Bach, J. A. Straseski, W. Clarke, Therapeutic drug monitoring in cancer chemotherapy. *Bioanalysis* **2**, 863–879 (2010).
3. V. T. DeVita, E. Chu, A history of cancer chemotherapy. *Cancer Res.* **68**, 8643–8653 (2008).
4. X. Huang, D. Wang, Z. Yuan, W. Xie, Y. Wu, R. Li, Y. Zhao, D. Luo, L. Cen, B. Chen, H. Wu, H. Xu, X. Sheng, M. Zhang, L. Zhao, L. Yin, A fully biodegradable battery for self-powered transient implants. *Small* **14**, e1800994 (2018).
5. J. D. Cohen, L. Li, Y. Wang, C. Thoburn, B. Afsari, L. Danilova, C. Douville, A. A. Javed, F. Wong, A. Mattox, R. H. Hruban, C. L. Wolfgang, M. G. Goggins, M. D. Molin, T. L. Wang, R. Roden, A. P. Klein, J. Ptak, L. Dobbyn, J. Schaefer, N. Silliman, M. Popoli, J. T. Vogelstein, J. D. Browne, R. E. Schoen, R. E. Brand, J. Tie, P. Gibbs, H. L. Wong, A. S. Mansfield, J. Jen, S. M. Hanash, M. Falconi, P. J. Allen, S. Zhou, C. Bettegowda, L. A. Diaz, C. Tomasetti, K. W. Kinzler, B. Vogelstein, A. M. Lennon, N. Papadopoulos, Detection and localization of surgically resectable cancers with a multi-analyte blood test. *Science* **359**, 926–930 (2018).
6. L. Wu, X. Qu, Cancer biomarker detection: Recent achievements and challenges. *Chem. Soc. Rev.* **44**, 2963–2997 (2015).
7. H. Jadvar, The use of imaging in the prediction and assessment of cancer treatment toxicity. *Diagnostics* **7**, 43 (2017).
8. M. Nematullah, Hasmatullah, A. Agnihotri, S. Kumar, A. Husain, M. A. Rahman, Evaluation of therapeutics' drug monitoring during cancer chemotherapy: A review. *Intell. Pharm.* **1**, 157–161 (2023).
9. E. Verscheure, I. Struys, M. Creta, K. Poels, J. Vanoirbeek, L. Lenaerts, F. Amant, M. Ghosh, L. Godderis, Development and validation of an UPLC-ESI-MS/MS method for simultaneous quantification of antineoplastic agents and their metabolites in human plasma after unintentional exposure. *Arch. Toxicol.* **99**, 259–270 (2025).
10. Y. Harahap, P. Ardiningsih, A. Corintias Winarti, D. J. Purwanto, Analysis of the doxorubicin and doxorubicinol in the plasma of breast cancer patients for monitoring the toxicity of doxorubicin. *Drug Des. Devel. Ther.* **14**, 3469–3475 (2020).
11. D. V. M. Sousa, F. V. Pereira, R. M. Orlando, Enhancing doxorubicin detection: Multiphase electroextraction for efficient and affordable UHPLC-DAD analysis in saliva. *Electrophoresis* **2024**, 10.1002/elps.202400094 (2024).
12. S. Fogli, R. Danesi, F. Innocenti, A. Di Paolo, G. Bocci, C. Barbara, M. Del Tacca, An improved HPLC method for therapeutic drug monitoring of daunorubicin, idarubicin, doxorubicin, epirubicin, and their 13-dihydro metabolites in human plasma. *Ther. Drug Monit.* **21**, 367–375 (1999).
13. J.-W. Seo, K. Fu, S. Correa, M. Eisenstein, E. A. Appel, H. T. Soh, Real-time monitoring of drug pharmacokinetics within tumor tissue in live animals. *Sci. Adv.* **8**, eabk2901 (2022).
14. S. Mazzucchelli, A. Ravelli, F. Gigli, M. Minoli, F. Corsi, P. Ciuffreda, R. Ottria, LC–MS/MS method development for quantification of doxorubicin and its metabolite 13-hydroxy doxorubicin in mice biological matrices: Application to a pharmaco-delivery study. *Biomed. Chromatogr.* **31**, 32–47 (2017).
15. M. Protti, R. Mandrioli, L. Mercolini, Tutorial: Volumetric absorptive microsampling (VAMS). *Anal. Chim. Acta* **1046**, 32–47 (2019).
16. Y. Zhang, G. Lee, S. Li, Z. Hu, K. Zhao, J. A. Rogers, Advances in bioresorbable materials and electronics. *Chem. Rev.* **123**, 11722–11773 (2023).
17. A. A. La Mattina, S. Mariani, G. Barillaro, Bioresorbable materials on the rise: From electronic components and physical sensors to in vivo monitoring systems. *Adv. Sci.* **7**, 1902872 (2020).
18. H. Ryu, M. H. Seo, J. A. Rogers, Bioresorbable metals for biomedical applications: from mechanical components to electronic devices. *Adv. Healthc. Mater.* **10**, e2002236 (2021).
19. C. M. Boutry, L. Beker, Y. Kaizawa, C. Vassos, H. Tran, A. C. Hinckley, R. Pfattner, S. Niu, J. Li, J. Claverie, Z. Wang, J. Chang, P. M. Fox, Z. Bao, Biodegradable and flexible arterial-pulse sensor for the wireless monitoring of blood flow. *Nat. Biomed. Eng.* **3**, 47–57 (2019).
20. E. Song, J. Li, J. A. Rogers, Barrier materials for flexible bioelectronic implants with chronic stability—Current approaches and future directions. *APL Mater.* **7**, 050902 (2019).
21. S. M. Yang, J. H. Shim, H. U. Cho, T. M. Jang, G. J. Ko, J. Shim, T. H. Kim, J. Zhu, S. Park, Y. S. Kim, S. Y. Joung, J. C. Choe, J. W. Shin, J. H. Lee, Y. M. Kang, H. Cheng, Y. Jung, C. H. Lee, D. P. Jang, S. W. Hwang, Hetero-integration of silicon nanomembranes with 2D materials for bioresorbable, wireless neurochemical system. *Adv. Mater.* **34**, e2108203 (2022).
22. J. Shin, Z. Liu, W. Bai, Y. Liu, Y. Yan, Y. Xue, I. Kandela, M. Pezhouh, M. R. MacEwan, Y. Huang, W. Z. Ray, W. Zhou, J. A. Rogers, Bioresorbable optical sensor systems for monitoring of intracranial pressure and temperature. *Sci. Adv.* **5**, eaaw1899 (2019).
23. M. Corsi, A. Paghi, S. Mariani, G. Golinelli, A. Debrassi, G. Egri, G. Leo, E. Vandini, A. Vilella, L. Dähne, D. Giuliani, G. Barillaro, Bioresorbable nanostructured chemical sensor for monitoring of pH level in vivo. *Adv. Sci.* **9**, e2202062 (2022).
24. J. Liu, N. Liu, Y. Xu, M. Wu, H. Zhang, Y. Wang, Y. Yan, A. Hill, R. Song, Z. Xu, M. Park, Y. Wu, J. L. Ciatti, J. Gu, H. Luan, Y. Zhang, T. Yang, H. Y. Ahn, S. Li, W. Z. Ray, C. K. Franz, M. R. MacEwan, Y. Huang, C. W. Hammill, H. Wang, J. A. Rogers, Bioresorbable shape-adaptive structures for ultrasonic monitoring of deep-tissue homeostasis. *Science* **383**, 1096–1103 (2024).
25. S. Li, D. Lu, S. Li, J. Liu, Y. Xu, Y. Yan, J. Z. Rodriguez, H. Bai, R. Avila, S. Kang, X. Ni, H. Luan, H. Guo, W. Bai, C. Wu, X. Zhou, Z. Hu, M. A. Pet, C. W. Hammill, M. R. MacEwan, W. Z. Ray, Y. Huang, J. A. Rogers, Bioresorbable, wireless, passive sensors for continuous pH measurements and early detection of gastric leakage. *Sci. Adv.* **10**, 16–22 (2024).
26. J. Li, J. Liu, Z. Wu, X. Shang, Y. Li, W. Huo, X. Huang, Fully printed and self-compensated bioresorbable electrochemical devices based on galvanic coupling for continuous glucose monitoring. *Sci. Adv.* **9**, eadi3839 (2023).
27. H. S. Kim, S. M. Yang, T. M. Jang, N. Oh, H. S. Kim, S. W. Hwang, Bioresorbable silicon nanomembranes and iron catalyst nanoparticles for flexible, transient electrochemical dopamine monitors. *Adv. Healthc. Mater.* **7**, e1801071 (2018).
28. J. D. Harvey, R. M. Williams, K. M. Tully, H. A. Baker, Y. Shamay, D. A. Heller, An in vivo nanosensor measures compartmental doxorubicin exposure. *Nano Lett.* **19**, 4343–4354 (2019).
29. N. Arroyo-Currás, J. Somerson, P. A. Vieira, K. L. Ploense, T. E. Kippin, K. W. Plaxco, Real-time measurement of small molecules directly in awake, ambulatory animals. *Proc. Natl. Acad. Sci. U.S.A.* **114**, 645–650 (2017).
30. T. T. Pham, H. T. Nguyen, C. D. Phung, S. Pathak, S. Regmi, D. H. Ha, J. O. Kim, C. S. Yong, S. K. Kim, J. E. Choi, S. Yook, J. B. Park, J. H. Jeong, Targeted delivery of doxorubicin for the treatment of bone metastasis from breast cancer using alendronate-functionalized graphene oxide nanosheets. *J. Ind. Eng. Chem.* **76**, 310–317 (2019).
31. H. S. Al-malky, S. E. Al Harthi, A. M. M. Osman, Major obstacles to doxorubicin therapy: Cardiotoxicity and drug resistance. *J. Oncol. Pharm. Pract.* **26**, 434–444 (2020).
32. M. Cagel, E. Grotz, E. Bernabeu, M. A. Moretton, D. A. Chiappetta, Doxorubicin: Nanotechnological overviews from bench to bedside. *Drug Discov. Today* **22**, 270–281 (2017).
33. U. Kanwal, N. I. Bukhari, M. Ovais, N. Abass, K. Hussain, A. Raza, Advances in nano-delivery systems for doxorubicin: An updated insight. *J. Drug Target.* **26**, 296–310 (2018).
34. A. U. Buzdar, C. Marcus, G. R. Blumenschein, T. L. Smith, Early and delayed clinical cardiotoxicity of doxorubicin. *Cancer* **55**, 2761–2765 (1985).
35. A. Pugazhendhi, T. N. J. I. Edison, B. K. Velmurugan, J. A. Jacob, I. Karuppusamy, Toxicity of Doxorubicin (Dox) to different experimental organ systems. *Life Sci.* **200**, 26–30 (2018).
36. O. Tacar, P. Sriamornsak, C. R. Dass, Doxorubicin: An update on anticancer molecular action, toxicity and novel drug delivery systems. *J. Pharm. Pharmacol.* **65**, 157–170 (2013).
37. K. B. Wallace, Doxorubicin-induced cardiac mitochondrionopathy. *Pharmacol. Toxicol.* **93**, 105–115 (2003).
38. L. D. Cranmer, L. M. Hess, T. Sugihara, H. G. Muntz, Cardiac events among patients with sarcoma treated with doxorubicin by method of infusion: A real-world database study. *Cancer Rep.* **6**, e1681 (2023).
39. S. S. Bielack, R. Erttmann, K. Winkler, G. Landbeck, Doxorubicin: Effect of different schedules on toxicity and anti-tumor efficacy. *Eur. J. Cancer Clin. Oncol.* **25**, 873–882 (1989).
40. K. E. Adkins, D. A. Solimando, J. A. Waddell, Doxorubicin and dacarbazine (AD) regimen for soft tissue sarcomas. *Hosp. Pharm.* **50**, 194–198 (2015).
41. D. Agudelo, P. Bourassa, J. Bruneau, G. Bérubé, É. Asselin, H.-A. Tajmir-Riahi, Probing the binding sites of antibiotic drugs doxorubicin and N-(trifluoroacetyl) doxorubicin with human and bovine serum albumins. *PLOS ONE* **7**, e43814 (2012).
42. A. Paghi, M. Corsi, A. A. La Mattina, G. Egri, L. Dähne, G. Barillaro, Wireless and flexible optoelectronic system for in situ monitoring of vaginal pH using a bioresorbable fluorescence sensor. *Adv. Mater. Technol.* **8**, 2201600 (2023).
43. E. J. Anglin, L. Chen, W. R. Freeman, M. Sailor, Porous silicon in drug delivery devices and materials. *Adv. Drug Deliv. Rev.* **60**, 1266–1277 (2008).

44. T. Tieu, M. Alba, R. Elnathan, A. Cifuentes-Rius, N. H. Voelcker, Advances in porous silicon–based nanomaterials for diagnostic and therapeutic applications. *Adv. Ther.* **2**, 1800095 (2019).
45. A. Jane, R. Dronov, A. Hodges, N. H. Voelcker, Porous silicon biosensors on the advance. *Trends Biotechnol.* **27**, 230–239 (2009).
46. E. Mazzotta, T. Di Giulio, S. Mariani, M. Corsi, C. Malitesta, G. Barillaro, Vapor-phase synthesis of molecularly imprinted polymers on nanostructured materials at room-temperature. *Small* **19**, 2302274 (2023).
47. Y. Liang, J. Huang, P. Zang, J. Kim, W. Hu, Molecular layer deposition of APTES on silicon nanowire biosensors: Surface characterization, stability and pH response. *Appl. Surf. Sci.* **322**, 202–208 (2014).
48. X. C. Lo, J. Y. Li, M. T. Lee, D. J. Yao, Frequency shift of a SH-SAW biosensor with glutaraldehyde and 3-aminopropyltriethoxysilane functionalized films for detection of epidermal growth factor. *Biosensors* **10**, 92 (2020).
49. K. P. S. Dancil, D. P. Greiner, M. J. Sailor, A porous silicon optical biosensor: Detection of reversible binding of IgG to a protein A-modified surface. *J. Am. Chem. Soc.* **121**, 7925–7930 (1999).
50. S. Shah, A. Chandra, A. Kaur, N. Sabnis, A. Lacko, Z. Gryczynski, R. Fudala, I. Gryczynski, Fluorescence properties of doxorubicin in PBS buffer and PVA films. *J. Photochem. Photobiol. B* **170**, 65–69 (2017).
51. C. Bertucci, G. Ascoli, G. Uccello-Barretta, L. Di Bari, P. Salvadori, The binding of 5-fluorouracil to native and modified human serum albumin: UV, CD, and ^{1}H and ^{19}F NMR investigation. *J. Pharm. Biomed. Anal.* **13**, 1087–1093 (1995).
52. V. M. Gun'ko, V. V. Turov, T. V. Krupska, M. D. Tsapko, Interactions of human serum albumin with doxorubicin in different media. *Chem. Phys.* **483-484**, 26–34 (2017).
53. P. A. J. Speth, Q. G. C. M. Van Hoesel, C. Haanen, Drug disposition clinical pharmacokinetics of doxorubicin. *Drug Dispos.* **31**, 15–31 (1988).
54. G. Toffoli, M. Hadla, G. Corona, I. Caligiuri, S. Palazzolo, S. Semeraro, A. Gamini, V. Canzonieri, F. Rizzolio, Exosomal doxorubicin reduces the cardiac toxicity of doxorubicin. *Nanomedicine* **10**, 2963–2971 (2015).
55. I. A. Bauer, E. V. Dmitrienko, Investigating non-covalent interactions of human serum albumin with doxorubicin and folic acid. *Biochem. Moscow Suppl. Ser. B* **18**, 231–242 (2024).
56. I. Oshina, J. Spigulis, Beer–Lambert law for optical tissue diagnostics: Current state of the art and the main limitations. *J. Biomed. Opt.* **26**, 100901 (2021).
57. Y. Xia, J. Zhong, M. Zhao, Y. Tang, N. Han, L. Hua, T. Xu, C. Wang, B. Zhu, Galactose-modified selenium nanoparticles for targeted delivery of doxorubicin to hepatocellular carcinoma. *Drug Deliv.* **26**, 1–11 (2019).
58. P. B. Johansen, Doxorubicin pharmacokinetics after intravenous and intraperitoneal administration in the nude mouse. *Cancer Chemother. Pharmacol.* **5**, 267–270 (1981).
59. R. J. A. Sharp, J. A. Ewald, R. E. Kenward, Guidelines and recommendations. *Trans. Environ. Support Syst. Des. Glob. Solut.* **51**, 246–257 (2013).
60. A.-K. Kraeuter, P. C. Guest, Z. Sarnyai, "The open field test for measuring locomotor activity and anxiety-like behavior" in *Pre-Clinical Models* (Humana Press, 2019), vol. 1897, pp. 99–103.
61. E. Daini, S. Hagmeyer, C. A. De Benedictis, J. S. Cristóvão, M. Bodria, A. M. Ross, A. Raab, T. M. Boeckers, J. Feldmann, C. M. Gomes, M. Zoli, A. Vilella, A. M. Grabrucker, S100B dysregulation during brain development affects synaptic SHANK protein networks via alteration of zinc homeostasis. *Transl. Psychiatry* **11**, 562 (2021).
62. Y. Wan, N. A. Krueger, C. R. Ocier, P. Su, P. V. Braun, B. T. Cunningham, Resonant mode engineering of photonic crystal sensors clad with ultralow refractive index porous silicon dioxide. *Adv. Opt. Mater.* **5**, 1700605 (2017).
63. M. J. Sailor, *Porous Silicon in Practice: Preparation*, *Characterization and Applications* (Wiley, 2012).
64. A. H. Bretag, Synthetic interstial fluid for isolated mammalian tissue. *Life Sci.* **8**, 319–329 (1969).
65. L. M. Strambini, A. Longo, S. Scarano, T. Prescimone, I. Palchetti, M. Minunni, D. Giannessi, G. Barillaro, Self-powered microneedle-based biosensors for pain-free high-accuracy measurement of glycaemia in interstitial fluid. *Biosens. Bioelectron.* **66**, 162–168 (2015).
66. H. Isler, D. Schenk, J. Bernhard, S. Kleiser, F. Scholkmann, D. Ostojic, A. Kalyanov, L. Ahnen, M. Wolf, T. Karen, Absorption spectra of early stool from preterm infants need to be considered in abdominal NIRS oximetry. *Biomed. Opt. Express* **10**, 2784–2794 (2019).
67. Council of the European Economic Community (EEC), CEE Council 89 609; Italian DL 26/2014, no. 979/2020/PR (EEC, 2014).
68. E. T. Hayes, C. E. Hagan, L. Khoryati, M. A. Gavin, D. J. Campbell, Regulatory T cells maintain selective access to IL-2 and immune homeostasis despite substantially reduced CD25 function. *J. Immunol.* **205**, 2667–2678 (2020).
69. S. Cui, C. Wang, W. Bai, J. Li, Y. Pan, X. Huang, H. Yang, Z. Feng, Q. Xiang, L. Fei, L. Zheng, J. Huang, Q. Zhang, Y. Wu, Y. Chen, CD1d1 intrinsic signaling in macrophages controls NLRP3 inflammasome expression during inflammation. *Sci. Adv.* **6**, eaaz7290 (2020).
70. L. Giannessi, M. G. Lupo, I. Rossi, M. G. Martina, A. Vilella, M. Bodria, D. Giuliani, F. Zimetti, I. Zanotti, F. Potì, F. Bernini, N. Ferri, M. Radi, Identification of 4-amino-2-Pyridones as new potent PCSK9 inhibitors: From phenotypic hit discovery to in vivo tolerability. *Eur. J. Med. Chem.* **265**, 116063 (2024).
71. D. C. Rogers, J. Peters, J. E. Martin, S. Ball, S. J. Nicholson, A. S. Witherden, M. Hafezparast, J. Latcham, T. L. Robinson, C. A. Quilter, E. M. C. Fisher, SHIRPA, a protocol for behavioral assessment: Validation for longitudinal study of neurological dysfunction in mice. *Neurosci. Lett.* **306**, 89–92 (2001).

Acknowledgments

Funding: This work was supported by the European Union Horizon Europe programme through the RESORB project (grant no. 101046946, G. Barillaro and D.G.), the Italian Ministry of University and Research (MUR) through the "ForeLab" project at the Information Engineering Department of the University of Pisa (Departments of Excellence 2023-2027, G. Barillaro and S.S.), the Italian Ministry of University and Research (MUR) through the Departments of Excellence 2023-2027 at the Department of Medical and Surgical Science for Children and Adults of the University of Modena and Reggio Emilia (M.D.), and the European Union–NextGenerationEU through the Italian Ministry of University and Research (MUR) under the "HEAL ITALIA" project (PNRR–M4C2-I1.3 PE_00000019, G. Barillaro, M.D., and G. Grisendi). **Author contributions:** M.C.: Writing—original draft, investigation, writing—review and editing, methodology, data curation, validation, formal analysis, and visualization. E.M.: Investigation, writing—review and editing, methodology, data curation, validation, formal analysis, and visualization. S.S.: Investigation, writing—review and editing, methodology, data curation, validation, formal analysis, and visualization. E.V.: Investigation, writing—review and editing, methodology, data curation, validation, formal analysis, and visualization. E.D.: Investigation, writing—review and editing, data curation, formal analysis, and visualization. A.V.: Investigation, writing—review and editing, methodology, resources, validation, formal analysis, and visualization. G.L.: Investigation, writing—review and editing, and methodology. M.F.: Investigation, writing—review and editing, methodology, data curation, validation, and formal analysis. G. Grisendi: Investigation, writing—review and editing, and methodology. G. Golinelli: Investigation, writing—review and editing, and methodology. M.D.: Conceptualization, investigation, writing—review and editing, methodology, resources, funding acquisition, data curation, validation, supervision, formal analysis, and project administration. G. Bocci: Writing—review and editing, methodology, and supervision. D.G.: Conceptualization, investigation, writing—review and editing, methodology, resources, funding acquisition, validation, supervision, project administration, and visualization. G. Barillaro: Writing—original draft, conceptualization, writing—review and editing, methodology, resources, funding acquisition, data curation, validation, supervision, project administration, and visualization. **Competing interests:** M.C., E.M., and G. Barillaro are inventors on patent application 102024000008506 submitted by the University of Pisa that covers a device for the detection of drug. All authors declare that they have no other competing interests. **Data and materials availability:** All data needed to evaluate the conclusions in the paper are present in the paper and/or the Supplementary Materials.

Submitted 25 July 2024
Accepted 11 March 2025
Published 16 April 2025
10.1126/sciadv.ads0265